T

Junchao Wu[a,b] and Dongdong Wang[b,*]

[a]College of Civil Engineering, Huaqiao University, Xiamen, Fujian 361021, China

[b]Department of Civil Engineering, Xiamen University, Xiamen, Fujian 361005, China

Abstract

Thin shell problems ignore the shear deformations and this leads to a requirement of C1 continuous approximations. Meshfree methods equipped with high order smoothed shape functions is suitable for thin shell analysis, since the high order shape function can also suppress the membrane locking in thin shell problems. However, meshfree shape function always perform a natural rational property, this is a big challenge to meet integration consistency for traditional Gauss integration rule within Galerkin weak form, while integration consistency serves a key role in accuracy of Galerkin meshfree methods. In this work, we proposed a reproducing kernel gradient smoothing integration (RKGSI) algorithm for thin shell problems, while the first and second order smoothed gradients are constructed based upon reproducing kernel smoothing gradient framework, with the aid of this framework, the integration consistency becomes a natural property by a replacement between smoothed gradients and traditional gradients of shape functions in Galerkin weak form. The order of basis functions used in smoothed gradient is determined by ensuring the optimal order of error convergence respected to energy norm. The traditional costly second order gradients are totally eliminated in RKGSI formulation. To further increase the efficiency of proposed method, a set of integration schemes are developed for consistent assembly of stiffness matrix, force vector and smoothed gradients, where the number of integration points, which accompanied with calculation of traditional shape functions and their first order gradients, are minimized by a global point of view. It is evident that the smoothed gradients meets the reproducing consistency of gradients that can ensure the optimal convergence property. The numerical examples demonstrate the efficacy and efficiency of proposed method, while the RKGSI performs a comparable result in energy error with interpolation by meshfree approximations.

Keywords: Meshfree method; Thin shell analysis; Second order smoothed gradient; Integration consistency; Reproducing kernel gradient smoothing integration

---

*Corresponding author, Email: ddwang@xmu.edu.cn

1. Introduction

Thin shell is one of the most frequently used structure in engineering practice, where the thickness of this kind structure is often much smaller than its radius. With the Kirchhoff-Love hypothesis [1–3], the transverse shear deformation is eliminated in thin shell analysis, such that at least C^1 continuous shape functions are required within Galerkin methods. In static and dynamic simulation of structure, the conventional finite element methods [1,2] are one of the most popular approximation scheme, however the construction of C^1 continuity is still a big challenge for cell-based finite element methods. In last three decades, the meshfree methods [1–3] equipped high order smoothed shape functions have attracted significant research attention, while the meshfree shape functions are established based upon a set of scattered nodes and the high order continuity of shape functions is easily fulfilled even with low order basis function. For thin shell analysis, this high order meshfree approximations can also alleviate the membrane locking caused by the mismatched approximation order of membrane strain and bending strain [1]. Moreover, in general, the nodal-based meshfree approximations can release the burden of mesh distortion and have the flexibility of local refinement. Due to these advantages, a wide variety meshfree methods are proposed and have been applied to many scientific or engineering fields. Among of them, moving least squares (MLS) and reproducing kernel (RK) meshfree approximations built their shape functions by enforcing the so-call consistency conditions, where the consistency conditions require that the corresponding approximations should exactly reproduce every functions spanned by basis functions, and this conditions usually serve as a basic requirement for the error convergence of resolved Galerkin solutions [1]. However, the high order smoothed meshfree shape functions accompany with the severely overlapping supports, which leads to a misalignment between numerical integration domains and supports of shape functions. As a result, the meshfree shape functions usually exhibit a piecewise rational nature in each integration domains, and it brings a serious difficulty to the accurate numerical integration in Galerkin weak forms [1].

a meshfree thin shell method for non-linear dynamic fracture rabczuk

a meshfree hermite-type duradial point interpolation liu

A gradient reproducing kernel based stabilized collocation method for the static and dynamic problems of thin elastic beams and plates wang lihua21

Gauss integration rules widely used in traditional finite element methods [1] are firstly introduced into Galerkin meshfree methods, while the problem domain is partitioned into a set of background integration cells. In each cells, since the integrands in Galerkin weak form is constructed by the piecewise rational meshfree shape functions, even the high order Gauss integration rule cannot exactly evaluate these integrands. In additional, too much Gauss integration points also leads to a low efficiency. For efficiency purpose, the nodal integration rules [1] are also frequently used herein, where the distributed meshfree nodes used for approximations are also regarded as integration points, such that it is a true "meshless" method since the background cells are no longer needed. However, the number of nodal integration points are not sufficient especially for high order basis approximations, adding auxiliary points around meshfree nodes, namely stress points, can improve the stability of nodal integrations, but the accuracy still remains at a low level. To obtain the continuous shape functions in every background cells, the support integration rule is established while the boundaries of shape function supports and integration cells are aligned. Along this path, the accuracy of Galerkin meshfree methods is improved, however, the high order Gauss integration rules mismatched the basis order are always employed to reduce the integration error and remain an optimal error convergence. The underneath reason of this context is the loss of integration consistency caused by non-polynomial meshfree shape functions. The conditions for checking integration consistency, namely integration constraint, is that the Galerkin methods implemented by particular integration rules can exactly reproduce the solution spanned by meshfree basis functions. It is equivalent to pass the traditional patch test in finite element methods. The systematical study of error estimates considered integration consistency is presented by Wang and Wu, where it was shown that the error of Galerkin meshfree methods are simultaneously controlled by reproducing consistency and integration consistency.

Recent years, various consistent integration rules are developed for satisfying the integration constraints, the linear integration constraint is proposed by Chen et al., and the gradients of shape functions evaluated at nodal integration points are reconstructed by a smoothed technique for meeting this linear integration constraint. The integration constraints are extended to second and higher order meshfree approximations by Duan et al, and then a quadratically consistent meshfree integration rules was proposed, which the gradients at Gauss points are rebuilt by fulfillment of high order integration

constraint. Accordingly, the number of integration points used in QCI should be coincide with the number of integration constraints. The residual error of SCNI has been studied by Wang and Wu, and a nesting sub-domain gradient smoothing integration algorithm are proposed to eliminate the second order term of this residual error. This approach optimally combined the stiffness matrices constructed by SCNI in a set of two-level triangular domains, but its extensions to higher order basis or three-dimensional case are still challenges. In contrast to reconstruct gradients of shape functions at integration points, Chen et al. presented an arbitrary order variationally consistent integration (VCI), in which various integration rules, such as Gauss integrations, nodal integrations and so on, are corrected to fulfill the integration constraints with modified test functions. However, the different approximations are applied for test functions and trail functions leads to a non-symmetric stiffness, which increase the costed time to solve linear functions. Recently, Wang and Wu developed a reproducing kernel gradient smoothed framework for naturally embedding the integration constraints into smoothed gradients, and thus the traditional Gauss integration rules matched the order of basis functions can be successfully used within Galerkin meshfree weak form with a maintenance of optimal error convergence. This approach namely reproducing kernel gradient smoothing integration (RKGSI) substitutes continuous and low order smoothed gradients for costly gradients of meshfree shape functions. Moreover, in order to reduce the calculations of meshfree shape functions from a global point of view, a minimization algorithm is designated to establish integration rules for construction of smoothed gradients. Meantime, RKGSI covers SCNI when the linear basis is used, and it is a general and efficient tool for Galerkin meshfree methods.

With the Kirchhoff-Love hypothesis, the second or higher order basis functions are needed for satisfaction of reproducing consistency of bending strains, and high order basis function can also release membrane locking. However, these high order approximations also bring a more severe difficulty to fulfill the integration consistency. The MLS and RK approximation is firstly introduced to thin shell linear and nonlinear meshfree formulations [1,2], in which the 6×6 Gauss points are employed in each quadrilateral integration cells and this will also bring a low efficiency. To satisfy the integration consistency, a sub-domain stabilized conforming integration algorithm proposed by Wang and Chen is introduced to thin plate problems, where the nodal based cells is divided into series of sub-domains for improving stability, and in each

sub-domains, the smoothing operation is used for construction of smoothed curvature to meet the quadratic integration constraint of thin plate problems. With the similar path, various smoothed meshfree formulations are proposed for thin plate or thin shell problems, e.g., a smoothed Hermite radial point method is proposed by Cui et al. [1] for thin plate problems, a smoothed maximum-entropy meshfree method is developed by Millán et al [1]. For higher order basis functions, the QCI with the second order smoothed gradients is proposed by Wang et al. for strain gradient elasticity problem, like with thin shell problems, the integration consistency of strain gradient elasticity problems also relates to first and second order gradients of shape functions. However, since the domain integration points are different for construction of first and second order gradients, under this circumstance, the QCI is not suitable for thin shell problems while the different domain integration schemes will lead to a failure for meeting integration consistency. Up to date, lots of consistent integration rules are developed to construct second order smoothed gradients for various problems. However, is still unknown.

In this work, we proposed an efficient and consistent numerical integration algorithm for thin shell meshfree formulations. The proposed method is established based upon reproducing kernel gradient smoothing framework, while the integration consistency for thin shell problems can be easily plugged into the construction of smoothed gradients. The integration consistency is derived during estimating the orthogonality of thin shell problems, since the orthogonality plays an important role in the accuracy analysis of Galerkin methods. It is turns out that the integration consistency of thin shell problems is no longer the condition that Galerkin weak forms exactly solve the solution spanned by basis functions, instead that, the integration consistency is a condition ensured the optimal error convergence of energy norm. The conventional Gauss integration schemes only meets the linear integration consistency of second order gradients, nonetheless this condition can be fulfilled without any condition. Subsequently, with the aid of reproducing kernel smoothing framework, the integration consistency become a natural property for first and second order gradients, and the costly traditional first and second order gradients of shape functions are replaced by smoothed gradients in Galerkin weak form. As a result, the low order Gauss integration rule matched the order of basis function can be successfully adopted for maintaining the optimal error convergence in Galerkin meshfree weak form. Furthermore, a series of integration schemes are designated for constructions of stiffness matrices, force vectors and RK smoothed

gradients, while the total calculation of traditional meshfree shape functions and their first order gradients is minimized with a global point of view during the whole procedure of analysis. The proposed RKGSI methods perform both high accuracy and efficiency comparing to traditional Gauss integration rules in numerical examples.

The reminder of this paper is listed as follows. Section 2 reviews the preliminaries about thin shell theory and Galerkin meshfree methods. The energy error estimate accounting to numerical integration has been studied in section 3, where a particular integration consistency for thin shell analysis is derived. Subsequently, the first and second order smoothed gradients with quadratic, cubic and quartic bases are constructed based upon reproducing kernel smoothing gradient framework in section 4, while all of the gradients naturally equip with integration consistency of thin shell problems. Numerical examples are presented in Section 5, which demonstrate the effectiveness and efficiency of the proposed methods. Finally, the conclusions and remarks are given in Section 6.

2. Kinematics and Galerkin Meshfree Methods

2.1 Kinematics for linear shell theory

Consider the configuration of a shell $\overline{\Omega}$, as shown in Fig. 1, which can be easily described by a parametric curvilinear coordinate system $\boldsymbol{\xi} = \{\xi^i\}_{i=1,2,3}$. The mid-surface of the shell is specified by the in-plane coordinates $\{\xi^\alpha\}_{\alpha=1,2}$, as the thickness direction of shell is by ξ^3, $-\frac{h}{2} \leq \xi^3 \leq \frac{h}{2}$, h is the thick of shell. In this work, Latin indices take the values from 1 to 3, and Greek indices are evaluated by 1 or 2. For the Kirchhoff-Love hypothesis[1], the position $\boldsymbol{x} \in \overline{\Omega}$ are defined by linear functions with respect to ξ^3:

$$\boldsymbol{x}(\xi^1, \xi^2, \xi^3) = \boldsymbol{r}(\xi^1, \xi^2) + \xi^3 \boldsymbol{a}_3(\xi^1, \xi^2) \tag{1}$$

in which $\boldsymbol{r}$ means the position on the mid-surface of shell, and $\boldsymbol{a}_3$ is corresponding normal direction. For the mid-surface of shell, the in-plane covariant base vector with respect to ξ^α can be derived by a trivial partial differentiation to $\boldsymbol{r}$:

$$\boldsymbol{a}_\alpha = \frac{\partial \boldsymbol{r}}{\partial \xi^\alpha} = \boldsymbol{r}_{,\alpha}, \quad \alpha = 1, 2 \tag{2}$$

for a clear expression, the subscript comma denotes the partial differentiation operation with respect to in-plane coordinates ξ^α. Thus, the normal vector $\boldsymbol{a}_3$ can be obtained by the normalized cross product of $\boldsymbol{a}_\alpha$'s, as follow:

$$\boldsymbol{a}_3 = \frac{\boldsymbol{a}_1 \times \boldsymbol{a}_2}{\|\boldsymbol{a}_1 \times \boldsymbol{a}_2\|} \tag{3}$$

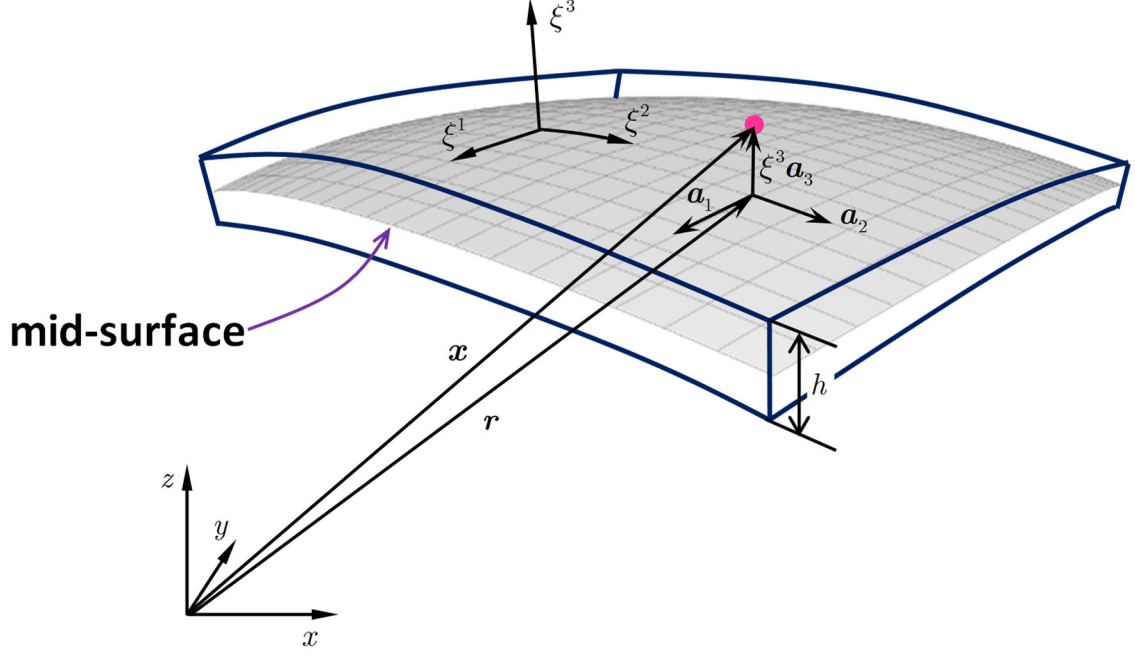where $\|\bullet\|$ is the Euclidean norm operator.

Figure 1 Configuration of the shell domain

With the assumption of infinitesimal deformation, the strain components with respect to global contravariant base have the form that:

$$\epsilon_{ij} = \frac{1}{2}(\boldsymbol{g}_i \cdot \boldsymbol{u}_{,j} + \boldsymbol{u}_{,i} \cdot \boldsymbol{g}_j) \tag{4}$$

where $\boldsymbol{g}_i$ is the global covariant base vector, which is similarly given by a partial differentiation of global position $\boldsymbol{x}$ with respect to ξ^i:

$$\begin{cases} \boldsymbol{g}_1 = \boldsymbol{x}_{,1} = \boldsymbol{a}_1 + \xi^3 \boldsymbol{a}_{3,1} \\ \boldsymbol{g}_2 = \boldsymbol{x}_{,2} = \boldsymbol{a}_2 + \xi^3 \boldsymbol{a}_{3,2} \\ \boldsymbol{g}_3 = \boldsymbol{x}_{,3} = \boldsymbol{a}_3 \end{cases} \tag{5}$$

and $\boldsymbol{u}(\xi^1, \xi^2, \xi^3)$ is the displacement for shell deformation. To fulfillment with Kirchhoff-Love hypothesis, the Tylor's expansion with respect to ξ^3 is introduced to displacement $\boldsymbol{u}$, yields:

$$\begin{aligned} \boldsymbol{u}(\xi^1, \xi^2, \xi^3) &= \boldsymbol{u}(\xi^1, \xi^2, 0) + \boldsymbol{u}_{,3}(\xi^1, \xi^2, 0)\xi^3 + \frac{1}{2}\boldsymbol{u}_{,3}(\xi^1, \xi^2, 0)(\xi^3)^2 + \cdots \\ &\approx \boldsymbol{v}(\xi^1, \xi^2) + \boldsymbol{\varphi}(\xi^1, \xi^2)\xi^3 \end{aligned} \tag{6}$$

where the quadratic and higher order terms are neglected. $\boldsymbol{v}$, $\boldsymbol{\varphi}$ represent the displacement and rotation of mid-surface, which are expressed as:

$$\boldsymbol{v}(\xi^1, \xi^2) = \boldsymbol{u}(\xi^1, \xi^2, 0), \quad \boldsymbol{\varphi}(\xi^1, \xi^2) = \boldsymbol{u}_{,3}(\xi^1, \xi^2, 0) \tag{7}$$

8

Subsequently, plugging Eqs. (5)-(7) into (4) and neglecting quadratic terms, the strains can be rewritten as follows:

$$\begin{aligned}
\epsilon_{\alpha\beta} &= \frac{1}{2}(g_\alpha \cdot u_{,\beta} + u_{,\alpha} \cdot g_\beta) \\
&\approx \frac{1}{2}(a_\alpha \cdot v_{,\beta} + v_{,\alpha} \cdot a_\beta) + \frac{1}{2}(a_{3,\alpha} \cdot v_{,\beta} + v_{,\alpha} \cdot a_{3,\beta} + a_\alpha \cdot \varphi_{,\beta} + \varphi_{,\alpha} \cdot a_\beta)\xi^3 \\
&= \varepsilon_{\alpha\beta} + \kappa_{\alpha\beta}\xi^3
\end{aligned} \tag{8}$$

$$\epsilon_{\alpha 3} = \frac{1}{2}(g_\alpha \cdot u_{,3} + u_{,\alpha} \cdot g_3) = \frac{1}{2}(a_\alpha \cdot \varphi + v_{,\alpha} \cdot a_3) + \frac{1}{2}(a_3 \cdot \varphi)_{,\alpha}\xi^3 \tag{9}$$

$$\epsilon_{33} = g_3 \cdot u_{,3} = a_3 \cdot \varphi \tag{10}$$

in which $\varepsilon_{\alpha\beta}$, $\kappa_{\alpha\beta}$ are membrane and bending strains respectively, which have the expressions as follows:

$$\varepsilon_{\alpha\beta} = \frac{1}{2}(a_\alpha \cdot v_{,\beta} + v_{,\alpha} \cdot a_\beta) \tag{11}$$

$$\kappa_{\alpha\beta} = \frac{1}{2}(a_{3,\alpha} \cdot v_{,\beta} + v_{,\alpha} \cdot a_{3,\beta} + a_\alpha \cdot \varphi_{,\beta} + \varphi_{,\alpha} \cdot a_\beta) \tag{12}$$

With the Kirchhoff-Love hypothesis, the thickness of the shell will not change during the deformation, and the strains related by direction of ξ^3 will be vanished, i.e. $\varepsilon_{i3} = 0$. As a result, the rotation φ is determined by enforcement of $\varepsilon_{i3} = 0$:

$$\varepsilon_{i3} = 0 \rightarrow \begin{cases} \varphi \cdot a_\alpha = -v_{,\alpha} \cdot a_3 \\ \varphi \cdot a_3 = 0 \end{cases} \rightarrow \varphi = -v_{,\alpha} \cdot a_3 a^\alpha \tag{13}$$

where a^α's are the in-plane contravariant base vectors. Substituting Eq. (13) into Eq. (12) can obtain that:

$$\kappa_{\alpha\beta} = (\Gamma^\gamma_{\alpha\beta} v_{,\gamma} - v_{,\alpha\beta}) \cdot a_3 \tag{14}$$

where $\Gamma^\gamma_{\alpha\beta} = r_{,\alpha\beta} \cdot a^\gamma$ is namely Christoffel symbol of the second kind. The detail derivation of (14) is given in Appendix. It is noted that, with the assumption of Kirchhoff-Love hypothesis, the transverse normal stress σ^{33}

2.2 Reproducing kernel (RK) approximation

In meshfree approximation, the mid-surface of the shell Ω is discretized by a set of meshfree nodes $\{\xi_I\}_{I=1}^{n_p}$ in parametric configuration, where n_p is the total number of

meshfree nodes. Furthermore, every meshfree nodes equips a meshfree shape function $\Psi_I(\boldsymbol{\xi})$, where the subscript I means it belongs to meshfree node $\boldsymbol{\xi}_I$. Then, the approximant of displacement namely $\boldsymbol{v}^h$ can be expressed by:

$$\boldsymbol{v}^h(\xi^1,\xi^2)=\sum_{I=1}^{n_p}\Psi_I(\xi^1,\xi^2)\boldsymbol{d}_I \tag{15}$$

in which $\boldsymbol{d}_I=\{d_{1I},d_{2I}\}^T$ is the undetermined coefficient vector at node $\boldsymbol{\xi}_I$. For a convenience of further development, we define the following meshfree space as:

$$V^h=span\{\Psi_I\}_{I=1}^{n_p} \tag{16}$$

In this study, the reproducing kernel approximation[] are used, and we can assume the shape function Ψ_I takes the form that:

$$\Psi_I(\xi^1,\xi^2)=\boldsymbol{p}^{[p]T}(\boldsymbol{\xi}_I-\boldsymbol{\xi})\boldsymbol{c}(\boldsymbol{\xi})\phi(\boldsymbol{\xi}_I-\boldsymbol{\xi}) \tag{17}$$

where $\boldsymbol{p}$ is the p-th order basis function vector:

$$\boldsymbol{p}^{[p]}=\{1,\xi^1,\xi^2,(\xi^1)^2,\xi^1\xi^2,...,(\xi^1)^i(\xi^2)^j,...,(\xi^2)^p\}^T, \quad 0\leq i+j\leq p \tag{18}$$

$\phi(\boldsymbol{\xi}_I-\boldsymbol{\xi})$ is the kernel function, which controls the support of meshfree shape function. As the quartic basis function has been studied in the numerical examples present in Section 5, the quantic B-spline function[] with a tensor product are chosen herein as the kernel function to insure the continuity of shape functions:

$$\phi(\boldsymbol{\xi}_I-\boldsymbol{\xi})=\phi(s_1)\phi(s_2), \quad s_\alpha=\frac{\left|\xi_I^\alpha-\xi^\alpha\right|}{s_{\alpha I}} \tag{19}$$

with:

$$\phi(s_\alpha)=\frac{1}{5!}\begin{cases}(3-3s_\alpha)^5-6(2-3s_\alpha)^5+15(1-3s_\alpha)^5, & s_\alpha\leq\frac{1}{3}\\(3-3s_\alpha)^5-6(2-3s_\alpha)^5, & \frac{1}{3}<s_\alpha\leq\frac{2}{3}\\(3-3s_\alpha)^5, & \frac{2}{3}<s_\alpha\leq1\\0, & s_\alpha>1\end{cases} \tag{20}$$

and $s_{\alpha I}$ means the support size of meshfree shape function Ψ_I. The unknown vector $\boldsymbol{c}$ in shape function are determined by the fulfillment of the so-call p-th order consistency condition:

$$\sum_{I=1}^{n_p}\Psi_I(\boldsymbol{\xi})\boldsymbol{p}^{[p]}(\boldsymbol{\xi}_I)=\boldsymbol{p}^{[p]}(\boldsymbol{\xi}) \tag{21}$$

or equivalently:

$$\sum_{I=1}^{n_p} \Psi_I(\boldsymbol{\xi}) \boldsymbol{p}^{[p]}(\boldsymbol{\xi}_I - \boldsymbol{\xi}) = \boldsymbol{p}^{[p]}(\boldsymbol{0}) \tag{22}$$

Substituting Eq. (17) into (22), we have:

$$\boldsymbol{A}(\boldsymbol{\xi})\boldsymbol{c}(\boldsymbol{\xi}) = \boldsymbol{p}^{[p]}(\boldsymbol{0}) \tag{23}$$

where $\boldsymbol{A}$ is called by moment matrix and has the form that:

$$\boldsymbol{A}(\boldsymbol{\xi}) = \sum_{I=1}^{n_p} \phi(\boldsymbol{\xi}_I - \boldsymbol{\xi}) \boldsymbol{p}^{[p]}(\boldsymbol{\xi}_I - \boldsymbol{\xi}) \boldsymbol{p}^{[p]T}(\boldsymbol{\xi}_I - \boldsymbol{\xi}) \tag{24}$$

As a result of Eq. (23), we obtain $\boldsymbol{c}(\boldsymbol{\xi}) = \boldsymbol{A}^{-1}(\boldsymbol{\xi})\boldsymbol{p}^{[p]}(\boldsymbol{0})$ and the meshfree shape function in Eq. (17) can be rewritten by:

$$\Psi_I(\boldsymbol{\xi}) = \boldsymbol{p}^{[p]T}(\boldsymbol{\xi}_I - \boldsymbol{\xi}) \boldsymbol{A}^{-1}(\boldsymbol{\xi}) \boldsymbol{p}^{[p]}(\boldsymbol{0}) \phi(\boldsymbol{\xi}_I - \boldsymbol{\xi}) \tag{25}$$

As we can find in the expression of meshfree shape functions, the left hand side of consistency condition in Eq. (22) are trivially embedded into Eq. (25). Thus, if the support sizes of the shape functions are sufficient big for ensuring invertibility of moment matrix, which said a regular meshfree nodal distribution [], the consistency condition is always automatically fulfilled, and meshfree interpolation error estimate in H^k Hilbert space [1] is given by:

$$\left\| \boldsymbol{v} - \boldsymbol{v}^i \right\|_{H^k} \leq C s^{p-k+1} \left| \boldsymbol{v} \right|_{H^{p+1}}, \quad \forall k \leq p+1 \tag{26}$$

where $\boldsymbol{v} \in C^m$ is a sufficient smoothed variable with $m > p$, $\boldsymbol{v}^i$ is the corresponding meshfree interpolant evaluated by:

$$\boldsymbol{v}^i = \sum_{I=1}^{n_p} \Psi_I(\boldsymbol{\xi}) \boldsymbol{v}(\boldsymbol{\xi}_I) \tag{27}$$

and s is denoted as a characteristic support size of shape functions and has the following relationship:

$$C_0 \leq \frac{s_{\alpha I}}{s} \leq C_1 \tag{28}$$

This error estimate of meshfree interpolant in Eq. (26) is a key feature for the accuracy of Galerkin methods, while the accuracy will be bounded by interpolation error without consideration of integration error.

With the aid of the approximant displacement in Eq. (15), the membrane and bending strain can also be discretized as follows:

$$\boldsymbol{\varepsilon}^h = \sum_{I=1}^{n_p} \boldsymbol{B}_I^m \boldsymbol{d}_I, \quad \boldsymbol{B}_I^m = \begin{bmatrix} \Psi_{I,1} & 0 \\ 0 & \Psi_{I,2} \\ \Psi_{I,2} & \Psi_{I,1} \end{bmatrix} \begin{Bmatrix} \boldsymbol{a}_1^T \\ \boldsymbol{a}_2^T \end{Bmatrix} \tag{29}$$

$$\boldsymbol{\kappa}^h = \sum_{I=1}^{n_p} \boldsymbol{B}_I^b \boldsymbol{d}_I, \quad \boldsymbol{B}_I^b = \begin{Bmatrix} \Gamma_{11}^\gamma \Psi_{I,\gamma} - \Psi_{I,11} \\ \Gamma_{22}^\gamma \Psi_{I,\gamma} - \Psi_{I,22} \\ 2(\Gamma_{12}^\gamma \Psi_{I,\gamma} - \Psi_{I,12}) \end{Bmatrix} \boldsymbol{a}_3^T \tag{30}$$

in which $\boldsymbol{B}_I^m$ and $\boldsymbol{B}_I^b$ are membrane and bending gradient matrices respectively.

2.3 Galerkin meshfree weak form and its energy error estimates

The Galerkin weak form for shell problems is listed as follow, where the total potential energy has been integrated along thickness of shell:

$$\text{Find} \quad \boldsymbol{v} \in H^2 : \mathcal{A}(\delta\boldsymbol{v}, \boldsymbol{v}) = \mathcal{F}(\delta\boldsymbol{v}), \quad \forall \delta\boldsymbol{v} \in H^2 \tag{31}$$

with a bilinear form $\mathcal{A}$ and a linear form $\mathcal{F}$ given by:

$$\mathcal{A}(\delta\boldsymbol{v}, \boldsymbol{v}) := \int_\Omega (\delta\boldsymbol{\varepsilon} : \boldsymbol{N} + \delta\boldsymbol{\kappa} : \boldsymbol{M}) d\Omega \tag{32}$$

$$\mathcal{F}(\delta\boldsymbol{v}) := \int_{\Gamma^t} \delta\boldsymbol{v} \cdot \bar{\boldsymbol{t}} d\Gamma + \int_{\Gamma^m} \delta\boldsymbol{\varphi} \cdot \bar{\boldsymbol{m}} d\Gamma + \int_\Omega \delta\boldsymbol{v} \cdot \bar{\boldsymbol{b}} d\Omega \tag{33}$$

in which $\boldsymbol{N}$, $\boldsymbol{M}$ can be regarded as the in-plane force and bending moment, respectively. It is noted that, since the stresses in transverse normal strain is zero, i.e. $\varepsilon^{33} = 0$, and we eliminate the contribution of transverse normal stress in Galerkin weak form of Eq. (31). In this work, we just consider the isotropic elasticity and the in-plane force and bending moment can be rewritten as following matrix forms by Voigot convention [1,2]:

$$\boldsymbol{N} = \begin{Bmatrix} N^{11} \\ N^{22} \\ N^{12} \end{Bmatrix} = \frac{Eh}{1-\nu^2} \boldsymbol{D}\boldsymbol{\varepsilon}, \quad \boldsymbol{M} = \begin{Bmatrix} M^{11} \\ M^{22} \\ M^{12} \end{Bmatrix} = \frac{Eh^3}{12(1-\nu^2)} = \boldsymbol{D}\boldsymbol{\kappa} \tag{34}$$

where:

$$\boldsymbol{D} = \begin{bmatrix} a^{11}a^{11} & \nu a^{11}a^{22} + (1-\nu)a^{12}a^{12} & a^{11}a^{12} \\ & a^{22}a^{22} & a^{22}a^{12} \\ Sym. & & \frac{1}{2}((1-\nu)a^{11}a^{22} + (1+\nu)a^{12}a^{12}) \end{bmatrix} \tag{35}$$

And Γ^t, Γ^m represent natural boundaries with prescribed force $\bar{t}$ and moment $\bar{m}$. $\bar{b}$ is denoted as body force in mid-plane, according to divergence theorem [1], the prescribed external forces have the following relationships:

$$\begin{cases} \bar{t} = \boldsymbol{a}_\beta N^{\alpha\beta} n_\alpha + \boldsymbol{a}_3 \Gamma^\gamma_{\alpha\beta} M^{\alpha\beta} n_\gamma + (\boldsymbol{a}_3 M^{\alpha\beta})_{,\beta} n_\alpha \\ \bar{m} = \boldsymbol{a}_\alpha M^{\alpha\beta} n_\beta \\ \bar{b} = -(\boldsymbol{a}_\beta N^{\alpha\beta})_{,\alpha} - (\Gamma^\gamma_{\alpha\beta} \boldsymbol{a}_3 M^{\alpha\beta})_{,\gamma} - (\boldsymbol{a}_3 M^{\alpha\beta})_{,\alpha\beta} \end{cases} \tag{36}$$

The Galerkin formulation of Eq. (31) is designate to seek a function $\boldsymbol{v}^h \in V^h$ with a minimum of energy for shell problems [1]. Thus, the error estimate of energy norm is the most straightforward measure for the accuracy of Galerkin methods. The bilinear form of Eq. (32) in Galerkin weak form is a mapping $\mathcal{A}: H^2 \times H^2 \to \mathbb{R}$, where bilinear form satisfy the coercivity and continuity []:

$$\mathcal{A}(\boldsymbol{v}, \boldsymbol{v}) \geq \alpha \|\boldsymbol{v}\|^2_{H^2}, \quad \forall \boldsymbol{v} \in H^2 \tag{37}$$

$$\left| \mathcal{A}(\delta\boldsymbol{v}, \boldsymbol{v}) \right| \leq \gamma \|\delta\boldsymbol{v}\|_{H^2} \|\boldsymbol{v}\|_{H^2}, \quad \forall \delta\boldsymbol{v}, \boldsymbol{v} \in H^2 \tag{38}$$

Combining continuity in Eq. (38) and bilinear form in Eq. (32), the energy norm defined by bilinear form has the following relationship:

$$\|\boldsymbol{v}\|_{H^{Energy}} = \left| \frac{1}{2} \mathcal{A}(\boldsymbol{v}, \boldsymbol{v}) \right|^{1/2} \geq C \|\boldsymbol{v}\|_{H^2} \tag{39}$$

Plugging meshfree approximations of Eqs. (15), (29) and (30) into Eq. (31) leads to:

$$\text{Find} \quad \delta\boldsymbol{v}^h \in V^h : \mathcal{A}(\delta\boldsymbol{v}^h, \boldsymbol{v}^h) = \mathcal{F}(\delta\boldsymbol{v}^h), \quad \forall \delta\boldsymbol{v}^h \in V^h \tag{40}$$

or a matrix form of:

$$\boldsymbol{K}\boldsymbol{d} = \boldsymbol{f} \tag{41}$$

where $\boldsymbol{d}$ is the unknown displacement vector going to solved, $\boldsymbol{K}$ and $\boldsymbol{f}$ are stiffness matrix and force vector:

$$\boldsymbol{K} = \overset{n_p}{\underset{I,J=1}{\mathsf{A}}} [\boldsymbol{K}_{IJ}]; \quad \boldsymbol{f} = \overset{n_p}{\underset{I=1}{\mathsf{A}}} [\boldsymbol{f}_I]; \quad \boldsymbol{d} = \overset{n_p}{\underset{I=1}{\mathsf{A}}} [\boldsymbol{d}_I] \tag{42}$$

and A is a global assembly operator. The components of $\boldsymbol{K}_{IJ}$ and $\boldsymbol{f}_I$ are evaluated by:

$$\boldsymbol{K}_{IJ} = \frac{Eh}{1-\nu^2} \int_\Omega \boldsymbol{B}_I^{mT} \boldsymbol{D} \boldsymbol{B}_J^m d\Omega + \frac{Eh^3}{12(1-\nu^2)} \int_\Omega \boldsymbol{B}_I^{bT} \boldsymbol{D} \boldsymbol{B}_J^b d\Omega \tag{43}$$

$$\boldsymbol{f}_I = \int_{\Gamma^t} \Psi_I \overline{\boldsymbol{t}} d\Gamma - \int_{\Gamma^m} \Psi_{I,\alpha} \boldsymbol{a}_3 \boldsymbol{a}^\alpha \cdot \overline{\boldsymbol{m}} d\Gamma + \int_\Omega \Psi_I \overline{\boldsymbol{b}} d\Omega \tag{44}$$

Using Eq. (31) mise (40) leads to the orthogonality of Galerkin formulation:

$$\mathcal{A}(\delta \boldsymbol{v}^h, \boldsymbol{e}) = 0 \tag{45}$$

Consequently, with a combination of coercivity in Eq. (37), continuity in Eq. (38) and orthogonality in Eq. (45), the error estimate of energy can be derived by:

$$
\begin{aligned}
\|\boldsymbol{e}\|_{H^{Energy}}^2 &= \left| \frac{1}{2} \mathcal{A}(\boldsymbol{e}, \boldsymbol{e}) \right| \\
&= \left| \frac{1}{2} \mathcal{A}(\boldsymbol{v} - \boldsymbol{v}^h, \boldsymbol{v} - \boldsymbol{v}^h) + \frac{1}{2} \underbrace{\mathcal{A}(\boldsymbol{v}^h - \boldsymbol{v}^i, \boldsymbol{v} - \boldsymbol{v}^h)}_{0} \right| \\
&= \left| \frac{1}{2} \mathcal{A}(\boldsymbol{v} - \boldsymbol{v}^i, \boldsymbol{e}) \right| \leq C \|\boldsymbol{v} - \boldsymbol{v}^i\|_{H^2} \|\boldsymbol{e}\|_{H^2} \\
&\leq C \|\boldsymbol{v} - \boldsymbol{v}^i\|_{H^2} \|\boldsymbol{e}\|_{H^{Energy}}
\end{aligned}
\tag{46}
$$

substituting interpolation error of RK meshfree approximation in Eq. (26) into Eq. (46), the energy error estimate can be rewritten as:

$$\|\boldsymbol{e}\|_{H^{Energy}} \leq C \|\boldsymbol{v} - \boldsymbol{v}^i\|_{H^2} \leq C s^{p-1} |\boldsymbol{v}|_{H^{p+1}} \tag{47}$$

It is noted that

3. Numerical Integration and its effect to Energy Error Estimates

3.1 Gaussian integration scheme

For traditional Galerkin meshfree formulations, the Gauss integration (GI) is always used for assembling the stiffness matrix and force vector. As shown in Fig. , the mid-plane of shell is partitioned into a group of triangular background integration cells, Ω_C's, and $\Omega = \{\Omega_C\}_{C=1}^{n_C}$. n_C is the total number of integration cells. For convenience of numerical implement, the vertices of triangular cells always coincide with the meshfree nodes, as a result, the size of integration cells can measured by the characterized support size s. In each integration cells, the Gauss integration rule required Gaussian points to locate by triangular parametric domain, where an example of 3-point Gauss integration rule (GI-3) is given in Fig. .

For clarity, we list a particular domain integration in force vector of (33) as follow:

$$\int_\Omega^* \delta \boldsymbol{v} \cdot \overline{\boldsymbol{b}} d\Omega = \sum_{C=1}^{n_C} \int_{\Omega_C}^* \delta \boldsymbol{v} \cdot \overline{\boldsymbol{b}} d\Omega = \sum_{C=1}^{n_C} \sum_{G=1}^{n_G} \delta \boldsymbol{v}(\boldsymbol{\xi}_G) \cdot \overline{\boldsymbol{b}}(\boldsymbol{\xi}_G) J_C \varpi_G \tag{48}$$

where the superscript asterisk presents the operator implemented by numerical integration. $\boldsymbol{\xi}_G$'s and ϖ_G's are locations and weights of Gaussian points, and the corresponding number of Gaussian point is n_G. J_C denotes the Jacobian during mapping from curvilinear parametric domain to triangular parametric domain.

Integration consistency condition is a requirement for Galerkin discrete formulation to maintain the optimal convergence rate coincided with interpolation.

Due to the non-polynomiality of meshfree shape functions, t

With the consideration of numerical integration, the variational problem of Eq. (31) becomes:

$$\text{Find} \quad \delta \tilde{\boldsymbol{v}}^h \in V^h : \mathcal{A}^*(\delta \boldsymbol{v}^h, \tilde{\boldsymbol{v}}^h) = \mathcal{F}^*(\delta \boldsymbol{v}^h), \quad \forall \delta \boldsymbol{v}^h \in V^h \tag{49}$$

where the exact solution $\boldsymbol{v}$ is no longer

$$\mathcal{A}(\delta \boldsymbol{v}^h, \tilde{\boldsymbol{e}}) = \mathcal{A}(\delta \boldsymbol{v}^h, \boldsymbol{v} - \tilde{\boldsymbol{v}}^h) \neq 0 \tag{50}$$

3.2 Integration consistency condition

In the previous work [1], a error estimate for orthogonality of potential Galerkin meshfree formulations is established, where integration constraint [1–3] plays a very important role and determines the order convergence rate. Integration constraint is a condition that requires Galerkin methods to exactly reproduce any solution spanned by basis vector. However, for thin shell problems, since the coefficients in bilinear and linear forms of Eqs. (32) and (33) is not a constant yet, reproducing exactness for discrete Galerkin weak form is no longer meaningful. On the contrary, integration constraint for shell problem is redefined that it requires numerical integration to obtain an optimal convergence rate for discrete Galerkin meshfree formulation.

Firstly, with the definitions of (49) the orthogonality of (50) can be rewritten as:

$$
\begin{aligned}
\left| \mathcal{A}(\delta \boldsymbol{v}^h, \tilde{\boldsymbol{e}}) \right| &= \left| (\mathcal{A} - \mathcal{A}^*)(\delta \boldsymbol{v}^h, \tilde{\boldsymbol{e}}) + \mathcal{A}^*(\delta \boldsymbol{v}^h, \tilde{\boldsymbol{e}}) \right| \\
&= \left| (\mathcal{A} - \mathcal{A}^*)(\delta \boldsymbol{v}^h, \tilde{\boldsymbol{e}}) + \mathcal{A}^*(\delta \boldsymbol{v}^h, \boldsymbol{v}) - \mathcal{A}^*(\delta \boldsymbol{v}^h, \tilde{\boldsymbol{v}}^h) \right| \\
&= \left| (\mathcal{A} - \mathcal{A}^*)(\delta \boldsymbol{v}^h, \tilde{\boldsymbol{e}}) + \mathcal{A}^*(\delta \boldsymbol{v}^h, \boldsymbol{v}) - \mathcal{F}^*(\delta \boldsymbol{v}^h) \right| \\
&\leq \left| (\mathcal{A} - \mathcal{A}^*)(\delta \boldsymbol{v}^h, \tilde{\boldsymbol{e}}) \right| + \left| \mathcal{A}^*(\delta \boldsymbol{v}^h, \boldsymbol{v}) - \mathcal{F}^*(\delta \boldsymbol{v}^h) \right|
\end{aligned}
\tag{51}
$$

where the prescribed variables in $\mathcal{F}^*$ are evaluated by exact solution:

$$\mathcal{F}^*(\delta\boldsymbol{v}^h) = \int_\Gamma^* \delta\boldsymbol{v}^h \cdot \bar{\boldsymbol{t}} d\Gamma + \int_\Gamma^* \delta\boldsymbol{\varphi}^h \cdot \bar{\boldsymbol{m}} d\Gamma + \int_\Omega^* \delta\boldsymbol{v}^h \cdot \bar{\boldsymbol{b}} d\Omega$$

$$= \int_\Gamma^* \delta\boldsymbol{v}^h \cdot \boldsymbol{a}_\beta N^{\alpha\beta} n_\alpha d\Gamma - \int_\Omega^* \delta\boldsymbol{v}^h \cdot (\boldsymbol{a}_\beta N^{\alpha\beta})_{,\alpha} d\Omega$$

$$+ \int_\Gamma^* \delta\boldsymbol{v}^h \cdot \boldsymbol{a}_\beta N^{\alpha\beta} n_\alpha d\Gamma - \int_\Omega^* \delta\boldsymbol{v}^h \cdot (\Gamma^\gamma_{\alpha\beta} \boldsymbol{a}_3 M^{\alpha\beta})_{,\gamma} d\Omega \tag{52}$$

$$+ \int_\Gamma^* \delta\boldsymbol{v}^h \cdot (\boldsymbol{a}_3 M^{\alpha\beta})_{,\beta} n_\alpha d\Gamma - \int_\Gamma^* \delta\boldsymbol{v}^h_{,\alpha} \cdot \boldsymbol{a}_3 M^{\alpha\beta} n_\beta d\Gamma - \int_\Omega^* \delta\boldsymbol{v}^h \cdot (\boldsymbol{a}_3 M^{\alpha\beta})_{,\alpha\beta} d\Omega$$

According to the error estimate of integration [1,2], the first term of Eq. (51) is bounded by continuous form of bilinear form $\mathcal{A}$:

$$\left|(\mathcal{A} - \mathcal{A}^*)(\delta\boldsymbol{v}^h, \tilde{\boldsymbol{e}})\right| \leq C \left|\mathcal{A}(\delta\boldsymbol{v}^h, \tilde{\boldsymbol{e}})\right| \tag{53}$$

For further development, two useful inner product operators are defined as:

$$\begin{cases} \mathcal{D}_1(\delta\boldsymbol{v}, \boldsymbol{v}) = \int_\Omega \delta\boldsymbol{v}_{,\alpha} \cdot \boldsymbol{v} d\Omega - \int_\Gamma \delta\boldsymbol{v} \cdot \boldsymbol{v} n_\alpha d\Gamma + \int_\Omega \delta\boldsymbol{v} \cdot \boldsymbol{v}_{,\alpha} d\Omega \\ \mathcal{D}_2(\delta\boldsymbol{v}, \boldsymbol{v}) = \int_\Omega \delta\boldsymbol{v}_{,\alpha\beta} \cdot \boldsymbol{v} d\Omega - \int_\Gamma \delta\boldsymbol{v}_{,\alpha} \cdot \boldsymbol{v} n_\beta d\Omega + \int_\Gamma \delta\boldsymbol{v} \cdot \boldsymbol{v}_{,\beta} n_\alpha d\Omega - \int_\Omega \delta\boldsymbol{v} \cdot \boldsymbol{v}_{,\alpha\beta} d\Omega \end{cases} \tag{54}$$

and according to Gauss divergence theorem [1], for sufficient smoothed variables, the following relationships hold true:

$$\begin{cases} \mathcal{D}_1(\delta\boldsymbol{v}, \boldsymbol{v}) = 0, & \forall \delta\boldsymbol{v}, \boldsymbol{v} \in C^1 \\ \mathcal{D}_2(\delta\boldsymbol{v}, \boldsymbol{v}) = 0, & \forall \delta\boldsymbol{v}, \boldsymbol{v} \in C^2 \end{cases} \tag{55}$$

Thus, the second term of orthogonality in Eq. (51) can be expressed by Eq. (55):

$$\left|\mathcal{A}^*(\delta\boldsymbol{v}^h, \boldsymbol{v}) - \mathcal{F}^*(\delta\boldsymbol{v}^h)\right| = \left|\mathcal{D}_1^*(\delta\boldsymbol{v}, \boldsymbol{a}_\beta N^{\alpha\beta}) + \mathcal{D}_1^*(\delta\boldsymbol{v}, \Gamma^\gamma_{\alpha\beta} \boldsymbol{a}_3 M^{\alpha\beta}) - \mathcal{D}_2^*(\delta\boldsymbol{v}, \boldsymbol{a}_3 M^{\alpha\beta})\right|$$

$$\leq \left|\mathcal{D}_1^*(\delta\boldsymbol{v}, \boldsymbol{a}_\beta N^{\alpha\beta})\right| + \left|\mathcal{D}_1^*(\delta\boldsymbol{v}, \Gamma^\gamma_{\alpha\beta} \boldsymbol{a}_3 M^{\alpha\beta})\right| + \left|\mathcal{D}_2^*(\delta\boldsymbol{v}, \boldsymbol{a}_3 M^{\alpha\beta})\right| \tag{56}$$

For further development, we denote $\mathcal{T}^{[q]}\boldsymbol{v}$ as the q-th order Lagrange interpolant of variable $\boldsymbol{v}$ based upon the integration cells of Ω_C's, the corresponding interpolation error is given by:

$$\left\|\boldsymbol{v} - \mathcal{T}^{[q]}\boldsymbol{v}\right\|_{H^k} \leq C s^{q-k+1} |\boldsymbol{v}|_{H^{q+1}}, \quad \forall k \leq q+1 \tag{57}$$

Assuming that the following relation hold true:

$$\begin{cases} \mathcal{D}_1^*(\delta\boldsymbol{v}^h, \mathcal{T}^{[q_1-1]}(\boldsymbol{a}_\beta N^{\alpha\beta})) = 0 \\ \mathcal{D}_1^*(\delta\boldsymbol{v}^h, \mathcal{T}^{[q_1-1]}(\Gamma^\gamma_{\alpha\beta} \boldsymbol{a}_3 M^{\alpha\beta})) = 0, & \forall \delta\boldsymbol{v} \in V^h \\ \mathcal{D}_2^*(\delta\boldsymbol{v}^h, \mathcal{T}^{[q_2-2]}(\boldsymbol{a}_3 M^{\alpha\beta})) = 0 \end{cases} \tag{58}$$

Using the relationships of Eqs. (55) and (58) into Eq. (56), for instance, the first term

of Eq. (56) is written as:

$$\left|\mathcal{D}_1^*(\delta\boldsymbol{v}, \boldsymbol{a}_\beta N^{\alpha\beta})\right| = \left|\mathcal{D}_1^*(\delta\boldsymbol{v}, \boldsymbol{a}_\beta N^{\alpha\beta}) - \underbrace{\mathcal{D}_1^*(\delta\boldsymbol{v}, \mathcal{T}^{[q_1-1]}(\boldsymbol{a}_\beta N^{\alpha\beta}))}_{0}\right|$$

$$= \left|\mathcal{D}_1^*(\delta\boldsymbol{v}, \boldsymbol{a}_\beta N^{\alpha\beta} - \mathcal{T}^{q_1-1}(\boldsymbol{a}_\beta N^{\alpha\beta})) - \underbrace{\mathcal{D}_1(\delta\boldsymbol{v}, \boldsymbol{a}_\beta N^{\alpha\beta} - \mathcal{T}^{q_1-1}(\boldsymbol{a}_\beta N^{\alpha\beta}))}_{0}\right| \quad (59)$$

$$= \left|(\mathcal{D}_1 - \mathcal{D}_1^*)(\delta\boldsymbol{v}, \boldsymbol{a}_\beta N^{\alpha\beta} - \mathcal{T}^{q_1-1}(\boldsymbol{a}_\beta N^{\alpha\beta}))\right|$$

then, according to error estimate of integration [1] into Eq. (59), if the numerical integration rule used in Eq. (59) has the (q_1-1)th order accuracy, then:

$$\left|\mathcal{D}_1^*(\delta\boldsymbol{v}, \boldsymbol{a}_\beta N^{\alpha\beta})\right| = \left|(\mathcal{D}_1 - \mathcal{D}_1^*)(\delta\boldsymbol{v}, \boldsymbol{a}_\beta N^{\alpha\beta} - \mathcal{T}^{[q_1-1]}(\boldsymbol{a}_\beta N^{\alpha\beta}))\right|$$

$$\leq C \|\delta\boldsymbol{v}\|_{H^2} \left\|\boldsymbol{a}_\beta N^{\alpha\beta} - \mathcal{T}^{[q_1-1]}(\boldsymbol{a}_\beta N^{\alpha\beta}))\right\|_{L^2}$$

$$\leq C s^{q_1} \|\delta\boldsymbol{v}\|_{H^2} \left|\boldsymbol{a}_\beta N^{\alpha\beta}\right|_{H^{q_1}} \quad (60)$$

$$\leq C s^{q_1} \|\delta\boldsymbol{v}\|_{H^{Energy}} \left|\boldsymbol{v}\right|_{H^{q_1+1}}$$

Following the similar path of Eqs. (59) and (60), the second and third terms of Eq. (56) are bounded as:

$$\left|\mathcal{D}_1^*(\delta\boldsymbol{v}, \Gamma_{\alpha\beta}^\gamma \boldsymbol{a}_3 M^{\alpha\beta})\right| = \left|(\mathcal{D}_1 - \mathcal{D}_1^*)(\delta\boldsymbol{v}, \Gamma_{\alpha\beta}^\gamma \boldsymbol{a}_3 M^{\alpha\beta} - \mathcal{T}^{q_1-1}(\Gamma_{\alpha\beta}^\gamma \boldsymbol{a}_3 M^{\alpha\beta}))\right|$$

$$\leq C s^{q_1} \|\boldsymbol{v}^h\|_{H^2} \left|\Gamma_{\alpha\beta}^\gamma \boldsymbol{a}_3 M^{\alpha\beta}\right|_{H^{q_1}} \quad (61)$$

$$\leq C s^{q_1} \|\boldsymbol{v}^h\|_{H^{Energy}} \left|\boldsymbol{v}\right|_{H^{q_1+2}}$$

$$\left|\mathcal{D}_2^*(\delta\boldsymbol{v}, \boldsymbol{a}_3 M^{\alpha\beta})\right| = \left|(\mathcal{D}_2 - \mathcal{D}_2^*)(\delta\boldsymbol{v}, \boldsymbol{a}_3 M^{\alpha\beta} - \mathcal{T}^{q_2-2}(\boldsymbol{a}_3 M^{\alpha\beta}))\right|$$

$$\leq C s^{q_2-1} \|\boldsymbol{v}^h\|_{H^2} \left|\boldsymbol{a}_3 M^{\alpha\beta}\right|_{H^{q_2-1}} \quad (62)$$

$$\leq C s^{q_2-1} \|\boldsymbol{v}^h\|_{H^{Energy}} \left|\boldsymbol{v}\right|_{H^{q_2+1}}$$

With the combination of Eqs. (51), (53), (56) and (60)-(62), the error estimate of orthogonality can be obtain:

$$\left|\mathcal{A}(\delta\boldsymbol{v}^h, \tilde{\boldsymbol{e}})\right| \leq C_{q_1} s^{q_1} \|\boldsymbol{v}^h\|_{H^{Energy}} \left|\boldsymbol{v}\right|_{H^{q_1+2}} + C_{q_2} s^{q_2-1} \|\boldsymbol{v}^h\|_{H^{Energy}} \left|\boldsymbol{v}\right|_{H^{q_2+1}} \quad (63)$$

It is noted that the assumption of Eq. (58) is a key feature in the proposed error estimate of orthogonality, where the orders of q_1, q_2 determine the error convergence rate. Since $\mathcal{T}^{[q]}\boldsymbol{v} \in \mathcal{P}^{[q]}$, the conditions of Eq. (58) can be simplified as:

$$\begin{cases} \int_\Omega^* \Psi_{I,\alpha} \boldsymbol{p}^{[q_1-1]} d\Omega = \int_\Gamma^* \Psi_I \boldsymbol{p}^{[q_1-1]} n_\alpha d\Gamma - \int_\Omega^* \Psi_I \boldsymbol{p}_{,\alpha}^{[q_1-1]} d\Omega \\ \int_\Omega^* \Psi_{I,\alpha\beta} \boldsymbol{p}^{[q_2-2]} d\Omega = \int_\Gamma^* \Psi_{I,\alpha} \boldsymbol{p}^{[q_2-2]} n_\beta d\Gamma - \int_\Gamma^* \Psi_I \boldsymbol{p}_{,\beta}^{[q_2-2]} n_\alpha d\Gamma + \int_\Omega^* \Psi_I \boldsymbol{p}_{,\alpha\beta}^{[q_2-2]} d\Omega \end{cases} \quad (64)$$

The condition of Eq. (64) is namely integration consistency condition for shell problems.

3.3 H^{Energy} error estimate considered numerical integration effect

The energy error accounting to numerical integration can be portioned into two parts by triangle inequality [1]:

$$
\begin{aligned}
\left\|\tilde{\boldsymbol{e}}\right\|_{H^{Energy}} &= \left\|\boldsymbol{v}-\tilde{\boldsymbol{v}}^h\right\|_{H^{Energy}} \\
&= \left\|\boldsymbol{v}-\boldsymbol{v}^h+\boldsymbol{v}^h-\tilde{\boldsymbol{v}}^h\right\|_{H^{Energy}} \\
&\leq \left\|\boldsymbol{v}-\boldsymbol{v}^h\right\|_{H^{Energy}} + \left\|\boldsymbol{v}^h-\tilde{\boldsymbol{v}}^h\right\|_{H^{Energy}} \\
&= \left\|\boldsymbol{e}\right\|_{H^{Energy}} + \left\|\boldsymbol{\eta}\right\|_{H^{Energy}}
\end{aligned}
\tag{65}
$$

where $\boldsymbol{\eta}=\boldsymbol{v}^h-\tilde{\boldsymbol{v}}^h$. The first term of (65) has been listed in Eq. (47). Since $\boldsymbol{\eta}\in V^h$, based upon the orthogonality of Eq . (45), we have $\mathcal{A}(\boldsymbol{\eta},\boldsymbol{v}-\boldsymbol{v}^h)=0$ and the second term of Eq. (65) can be expressed as:

$$
\begin{aligned}
\left\|\boldsymbol{\eta}\right\|_{H^{Energy}}^2 &= \left|\frac{1}{2}\mathcal{A}(\boldsymbol{\eta},\boldsymbol{\eta})\right| \\
&= \left|\frac{1}{2}\mathcal{A}(\boldsymbol{\eta},\boldsymbol{v}^h-\tilde{\boldsymbol{v}}^h)+\frac{1}{2}\underbrace{\mathcal{A}(\boldsymbol{\eta},\boldsymbol{v}-\boldsymbol{v}^h)}_{0}\right| = \left|\frac{1}{2}\mathcal{A}(\boldsymbol{\eta},\tilde{\boldsymbol{e}})\right| \\
&\leq C_{q_1}s^{q_1}\left\|\boldsymbol{\eta}\right\|_{H^{Energy}}\left|\boldsymbol{v}\right|_{H^{q_1+2}} + C_{q_2}s^{q_2-1}\left\|\boldsymbol{\eta}\right\|_{H^{Energy}}\left|\boldsymbol{v}\right|_{H^{q_2+1}}
\end{aligned}
\tag{66}
$$

where the error estimate of orthogonality in Eq. (63) is used herein. As a result, the error estimate of energy norm with numerical integration effect can be given by:

$$
\left\|\tilde{\boldsymbol{e}}\right\|_{H^{Energy}} \leq C_p s^{p-1}\left|\boldsymbol{v}\right|_{H^{p+1}} + C_{q_1}s^{q_1}\left\|\boldsymbol{v}^h\right\|_{\boldsymbol{H}^2}\left|\boldsymbol{v}\right|_{\boldsymbol{H}^{q_1+2}} + C_{q_2}s^{q_2-1}\left\|\boldsymbol{v}^h\right\|_{\boldsymbol{H}^2}\left|\boldsymbol{v}\right|_{\boldsymbol{H}^{q_2+1}}
\tag{67}
$$

As we can find in Eq. (67), the error estimate of energy norm consists of three parts, one is interpolation error controlled by consistency condition, the other two are numerical integration error determined by integration consistency condition of first and second order gradients of shape functions. Once the order of basis function have been chosen, the most ideal numerical integration must satisfy with integration consistency with $q_1=p-1$, $q_2=p$, such that the integration scheme can maintain the optimal convergence rate of $p-1$ and be implemented more easily because of the low order of q_1, q_2. Furthermore, apparently, the conventional Galerkin meshfree used Gauss integration rules meet the integration consistency conditions with $q_1=0$, $q_2=1$. In order to eliminate the effect of integration error, the high order Gauss integration rules is adapted to lower the constants of C_{q_1}, C_{q_2} in Eq. (67). However, with the increase of meshfree nodes, the error of solution with Gauss integration rule will finally be

bounded by the error of numerical integration.

4. Reproducing Kernel Smoothed Membrane and Bending Strains

The reproducing kernel gradient smoothing framework [1] provides a convenient and general way to construct smoothed gradient with inherently integration consistency. Herein, we introduce to establish the first and second order gradients of shape functions to fulfill with the integration consistency conditions of Eq. (64) for a optimal convergence rate. In this framework, the first and second order smoothed gradient namely $\tilde{\Psi}_{I,\alpha}$, $\tilde{\Psi}_{I,\alpha\beta}$ are established in a generic integration cell Ω_C, and take the following reproducing kernel form [1]:

$$\begin{cases} \tilde{\Psi}_{I,\alpha}(\boldsymbol{\xi}) = \boldsymbol{p}^{[p-2]T}(\boldsymbol{\xi})\boldsymbol{G}^{-1}\boldsymbol{g}_{\alpha I} \\ \tilde{\Psi}_{I,\alpha\beta}(\boldsymbol{\xi}) = \boldsymbol{p}^{[p-2]T}(\boldsymbol{\xi})\boldsymbol{G}^{-1}\boldsymbol{g}_{\alpha\beta I} \end{cases}, \quad \boldsymbol{\xi} \in \Omega_C \tag{68}$$

where, as mentioned in previous section, the best economic orders of the fulfilling integration consistency condition are $q_1 = p-1$, $q_2 = p$. Obviously from Eq. (64), the orders of basis function used in first and second smoothed gradients are identically chosen as $p-2$. Accordingly, $\boldsymbol{g}_{\alpha I}$ and $\boldsymbol{g}_{\alpha\beta I}$ can be regarded as right-hand side of local integration consistency conditions and have the forms that:

$$\begin{cases} \boldsymbol{g}_{\alpha I} = \int_{\Gamma_C}^{*} \Psi_I \boldsymbol{p}^{[p-2]} n_\alpha d\Gamma - \int_{\Omega_C}^{*} \Psi_I \boldsymbol{p}_{,\alpha}^{[p-2]} d\Omega \\ \boldsymbol{g}_{\alpha\beta I} = \int_{\Gamma_C}^{*} \Psi_{I,\alpha} \boldsymbol{p}^{[p-2]} n_\beta d\Gamma - \int_{\Gamma_C}^{*} \Psi_I \boldsymbol{p}_{,\beta}^{[p-2]} n_\alpha d\Gamma + \int_{\Omega_C}^{*} \Psi_I \boldsymbol{p}_{,\alpha\beta}^{[p-2]} d\Omega \end{cases} \tag{69}$$

and the corresponding moment matrix $\boldsymbol{G}$ is evaluated by:

$$\boldsymbol{G} = \int_{\Omega_C}^{*} \boldsymbol{p}^{[p-2]}(\boldsymbol{\xi})\boldsymbol{p}^{[p-2]T}(\boldsymbol{\xi})d\Omega \tag{70}$$

With the aid of reproducing kernel gradient smoothing framework, the first and second order gradients of meshfree shape function can naturally meet the integration consistency of $q_1 = p-1$, $q_2 = p$, which can be easily verified by substituting Eq. (68) into (64):

$$\int_{\Omega}^{*} \tilde{\Psi}_{I,\alpha} \boldsymbol{p}^{[p-2]} d\Omega = \sum_{C=1}^{n_C} \int_{\Omega_C}^{*} \tilde{\Psi}_{I,\alpha} \boldsymbol{p}^{[p-2]} d\Omega$$

$$= \sum_{C=1}^{n_C} \underbrace{\int_{\Omega_C}^{*} \boldsymbol{p}^{[p-2]} \boldsymbol{p}^{[p-2]T} d\Omega}_{\boldsymbol{G}} \boldsymbol{G}^{-1} \boldsymbol{g}_{\alpha I} \tag{71}$$

$$= \sum_{C=1}^{n_C} \boldsymbol{g}_{\alpha I} = \int_{\Gamma}^{*} \Psi_I \boldsymbol{p}^{[p-2]} n_\alpha d\Gamma - \int_{\Omega}^{*} \Psi_I \boldsymbol{p}_{,\alpha}^{[p-2]} d\Omega$$

$$\int_{\Omega}^{*} \tilde{\Psi}_{I,\alpha\beta} \boldsymbol{p}^{[p-2]} d\Omega = \sum_{C=1}^{n_C} \int_{\Omega_C}^{*} \tilde{\Psi}_{I,\alpha\beta} \boldsymbol{p}^{[p-2]} d\Omega$$

$$= \sum_{C=1}^{n_C} \underbrace{\int_{\Omega_C}^{*} \boldsymbol{p}^{[p-2]} \boldsymbol{p}^{[p-2]T} d\Omega}_{\boldsymbol{G}} \boldsymbol{G}^{-1} \boldsymbol{g}_{\alpha\beta I} \tag{72}$$

$$= \sum_{C=1}^{n_C} \boldsymbol{g}_{\alpha\beta I} = \int_{\Gamma}^{*} \Psi_{I,\alpha} \boldsymbol{p}^{[p-2]} n_\beta d\Gamma - \int_{\Gamma}^{*} \Psi_I \boldsymbol{p}_{,\beta}^{[p-2]} n_\alpha d\Gamma + \int_{\Omega}^{*} \Psi_I \boldsymbol{p}_{,\alpha\beta}^{[p-2]} d\Omega$$

where the verifications of Eqs. (71), (72) implicitly require that $\boldsymbol{G}$ employs the same integration rules as those for the domain integration in $\boldsymbol{K}$, and $\boldsymbol{g}_{\alpha I}$, $\boldsymbol{g}_{\alpha\beta I}$ and $\boldsymbol{f}$ also use identical integration rules.

Subsequently, we use the first and second gradients of meshfree shape functions to approximate the membrane and bending strains of Eqs. (29), (30), yields:

$$\tilde{\boldsymbol{\varepsilon}}^h = \sum_{I=1}^{n_p} \tilde{\boldsymbol{B}}_I^m \boldsymbol{d}_I, \quad \tilde{\boldsymbol{B}}_I^m = \begin{bmatrix} \tilde{\Psi}_{I,1} & 0 \\ 0 & \tilde{\Psi}_{I,2} \\ \tilde{\Psi}_{I,2} & \tilde{\Psi}_{I,1} \end{bmatrix} \begin{Bmatrix} \boldsymbol{a}_1^T \\ \boldsymbol{a}_2^T \end{Bmatrix} \tag{73}$$

$$\tilde{\boldsymbol{\kappa}}^h = \sum_{I=1}^{n_p} \tilde{\boldsymbol{B}}_I^b \boldsymbol{d}_I, \quad \tilde{\boldsymbol{B}}_I^b = \begin{Bmatrix} \Gamma_{11}^\gamma \tilde{\Psi}_{I,\gamma} - \tilde{\Psi}_{I,11} \\ \Gamma_{22}^\gamma \tilde{\Psi}_{I,\gamma} - \tilde{\Psi}_{I,22} \\ 2(\Gamma_{12}^\gamma \tilde{\Psi}_{I,\gamma} - \tilde{\Psi}_{I,12}) \end{Bmatrix} \boldsymbol{a}_3^T \tag{74}$$

where $\tilde{\boldsymbol{\varepsilon}}^h$, $\tilde{\boldsymbol{\kappa}}^h$ are namely smoothed membrane strain and smoothed bending strain respectively, and $\tilde{\boldsymbol{B}}_I^m$, $\tilde{\boldsymbol{B}}_I^b$ are the corresponding smoothed gradient matrices. Furthermore, plugging Eqs. (73) and (74) into Eq. (43), the components of stiffness matrix $\boldsymbol{K}$ can be evaluated by:

$$\boldsymbol{K}_{IJ} = \frac{Eh}{1-\nu^2} \int_{\Omega}^{*} \tilde{\boldsymbol{B}}_{I}^{mT} \boldsymbol{D} \tilde{\boldsymbol{B}}_{J}^{m} d\Omega + \frac{Eh^3}{12(1-\nu^2)} \int_{\Omega}^{*} \tilde{\boldsymbol{B}}_{I}^{bT} \boldsymbol{D} \tilde{\boldsymbol{B}}_{J}^{b} d\Omega$$

$$= \frac{Eh}{1-\nu^2} \sum_{C=1}^{n_C} \int_{\Omega}^{*} \tilde{\boldsymbol{B}}_{I}^{mT} \boldsymbol{D} \tilde{\boldsymbol{B}}_{J}^{m} d\Omega + \frac{Eh^3}{12(1-\nu^2)} \sum_{C=1}^{n_C} \int_{\Omega}^{*} \tilde{\boldsymbol{B}}_{I}^{bT} \boldsymbol{D} \tilde{\boldsymbol{B}}_{J}^{b} d\Omega \qquad (75)$$

$$= \sum_{C=1}^{n_C} \sum_{G=1}^{n_G} \left(\begin{matrix} \dfrac{Eh}{1-\nu^2} \tilde{\boldsymbol{B}}_{I}^{mT}(\boldsymbol{\xi}_G) \boldsymbol{D}(\boldsymbol{\xi}_G) \tilde{\boldsymbol{B}}_{J}^{m}(\boldsymbol{\xi}_G) \\ + \dfrac{Eh^3}{12(1-\nu^2)} \tilde{\boldsymbol{B}}_{I}^{bT}(\boldsymbol{\xi}_G) \boldsymbol{D}(\boldsymbol{\xi}_G) \tilde{\boldsymbol{B}}_{J}^{b}(\boldsymbol{\xi}_G) \end{matrix} \right) J(\boldsymbol{\xi}_G) \varpi_G$$

where, as the naturally embedding of integration consistency, the domain integration in stiffness matrix can employ the normal Gauss integration rules used in finite element analysis, and this integration rule is also adopted for integration of moment matrix $\boldsymbol{G}$:

$$\boldsymbol{G} = \sum_{G=1}^{n_G} \boldsymbol{p}^{[p-2]}(\boldsymbol{\xi}_G) \boldsymbol{p}^{[p-2]T}(\boldsymbol{\xi}_G) J(\boldsymbol{\xi}_G) \varpi_G \qquad (76)$$

On the contrary, it is noted that the integration rules in force vector of Eq. (44) should be the same with the integration rules in $\boldsymbol{g}_{\alpha I}$, $\boldsymbol{g}_{\alpha\beta I}$ for the fulfillment of integration consistency, and these integration rules can be distinguish with that of $\boldsymbol{K}$, $\boldsymbol{G}$.

4.2 Efficient implement for smoothed gradients

In reproducing kernel gradient smoothing framework, the smoothed gradients can implement by an efficient way. As shown in expressions of smoothed gradients in Eqs. (68)-(70), the numerical implement of smoothed gradients based upon reproducing kernel gradient smoothing framework only uses meshfree shape functions and its first order gradients, and eliminates costly traditional second order gradients of meshfree shape functions. Moreover, in previous work [1], a set of explicit integration rules used in construction of reproducing kernel smoothed gradients is systematically developed, where the total number of sample points in these integration rules is minimized from a global point of view. Such that, the proposed RKGSI formulation can achieve the optimal error convergence rate with the lowest computation of traditional meshfree shape functions during assembly of stiffness matrix and force vector.

The explicit integration rules for construction of smoothed gradients are established by a two-step procedure as described in the work [1]: The first step is to minimize the sample points from a global point of view, and the second step is to determine the locations and weights of sample points by satisfying the reproducing consistency of smoothed gradient. Apparently, the reproducing consistency of smoothed gradient
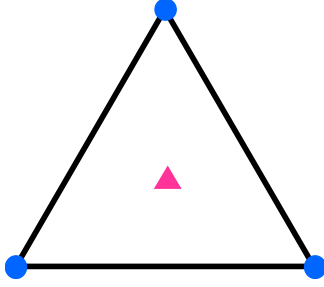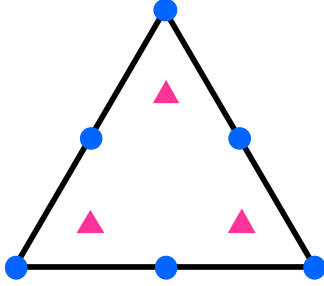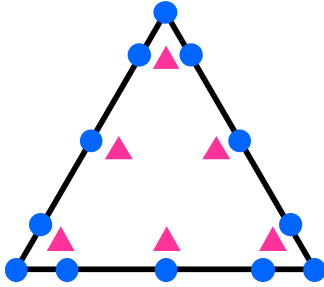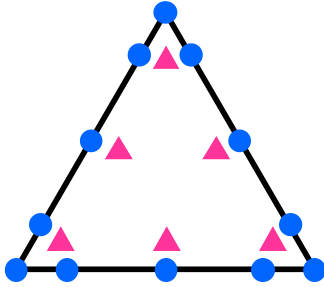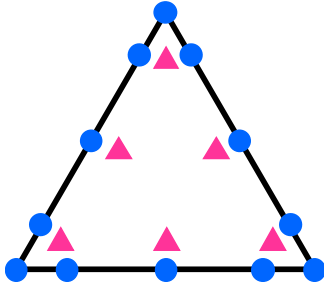
determines the integration accuracy for constructing smoothed gradients. Since the proposed first and second order smoothed gradients of Eq. (68) had the same order of basis function, i.e. $p-2$, the integration schemes developed for first order smoothed gradients[1] are also suitable for second order gradient. For instance, Table 1 presents the integration schemes for assembly of stiffness matrix, force vector and evaluations of smoothed gradients with quadratic, cubic and quartic basis functions, where the locations of integration points are depicted by triangular parametric coordinates η_i's:

$$\boldsymbol{\xi} = \boldsymbol{\xi}_1\eta_1 + \boldsymbol{\xi}_2\eta_2 + \boldsymbol{\xi}_3\eta_3, \quad \eta_1 + \eta_2 + \eta_3 = 1 \tag{77}$$

furthermore, $\langle \bullet \rangle$ denotes a permutation operator that gives all possible distinct combinations of the coordinate components, for clarity, a represent integration point $\hat{\boldsymbol{\xi}} = \langle \eta_a, \eta_b, \eta_c \rangle$ implies the following sets of integration points:

$$\begin{cases} \langle \eta_a, \eta_b, \eta_c \rangle : (\eta_a, \eta_b, \eta_c) & \text{for } \eta_a = \eta_b = \eta_c \\ \langle \eta_a, \eta_b, \eta_c \rangle : (\eta_a, \eta_b, \eta_c), (\eta_b, \eta_a, \eta_c), (\eta_b, \eta_c, \eta_a) & \text{for } \eta_a \neq \eta_b = \eta_c \\ \langle \eta_a, \eta_b, \eta_c \rangle : (\eta_a, \eta_b, \eta_c), (\eta_c, \eta_a, \eta_b), (\eta_b, \eta_c, \eta_a), & \\ \qquad (\eta_a, \eta_c, \eta_b), (\eta_c, \eta_b, \eta_a), (\eta_b, \eta_a, \eta_c) & \text{for } \eta_a \neq \eta_b \neq \eta_c \end{cases} \tag{78}$$

Table 1. Numerical integration schemes for construction of RKGSI

Basis order	Illustration	Integration scheme for RKGSI

$p = 2$

▲: Integration points for $\boldsymbol{K}$, $\boldsymbol{G}$

$\boldsymbol{\xi}_G$	ϖ_G
$\left\langle \frac{1}{3}, \frac{1}{3}, \frac{1}{3} \right\rangle$	1

●: Integration for $\boldsymbol{f}$, $\boldsymbol{g}_{\alpha I}$, $\boldsymbol{g}_{\alpha\beta I}$

$\boldsymbol{\xi}_S$	ϖ_S^b	ϖ_S^i
$\langle 1, 0, 0 \rangle$	$\frac{1}{2}$	$\frac{1}{3}$

$p = 3$

▲: Integration points for $\boldsymbol{K}$, $\boldsymbol{G}$

$\boldsymbol{\xi}_G$	ϖ_G
$\left\langle \frac{2}{3}, \frac{1}{6}, \frac{1}{6} \right\rangle$	$\frac{1}{3}$

●: Integration for $\boldsymbol{f}$, $\boldsymbol{g}_{\alpha I}$, $\boldsymbol{g}_{\alpha\beta I}$

$\boldsymbol{\xi}_S$	ϖ_S^b	ϖ_S^i
$\langle 1, 0, 0 \rangle$	$\frac{1}{6}$	0
$\left\langle \frac{1}{2}, \frac{1}{2}, 0 \right\rangle$	$\frac{2}{3}$	$\frac{1}{3}$

$p = 4$

▲: Integration points for $\boldsymbol{K}$, $\boldsymbol{G}$

$\boldsymbol{\xi}_G$	ϖ_G
$\langle \eta_a, \eta_b, \eta_b \rangle$	0.223381589678011
$\eta_a = 0.108103018168070$	
$\eta_b = 0.445948490915965$	
$\langle \eta_a, \eta_a, \eta_b \rangle$	0.109951743655322
$\eta_a = 0.816847572980459$	
$\eta_b = 0.091576213509771$	

●: Integration for $\boldsymbol{f}$, $\boldsymbol{g}_{\alpha I}$, $\boldsymbol{g}_{\alpha\beta I}$

$\boldsymbol{\xi}_S$	ϖ_S^b	ϖ_S^i
$\left\langle \frac{1}{3}, \frac{1}{3}, \frac{1}{3} \right\rangle$	0	$\frac{9}{20}$
$\langle 1, 0, 0 \rangle$	$\frac{1}{20}$	$-\frac{1}{30}$
$\left\langle \frac{1}{2}, \frac{1}{2}, 0 \right\rangle$	$\frac{16}{45}$	$\frac{4}{135}$
$\left\langle \frac{7+\sqrt{21}}{14}, \frac{7-\sqrt{21}}{14}, 0 \right\rangle$	$\frac{49}{180}$	$\frac{49}{540}$

As we can find in Table 1, the pink triangles stand for the integration points used in $\boldsymbol{K}$, $\boldsymbol{G}$, the detail evaluation is listed in Eqs. (75), (76). On the contrary, the blue cycles present the integration points for $\boldsymbol{f}$, $\boldsymbol{g}_{\alpha I}$, $\boldsymbol{g}_{\alpha\beta I}$, where $\boldsymbol{\xi}_S$'s are the locations of integration points, ϖ_S^b's and ϖ_S^i's denote the weights for boundary integration and domain integration respectively. For instance, using the proposed integration scheme in $\boldsymbol{g}_{\alpha I}$, $\boldsymbol{g}_{\alpha\beta I}$ leads to:

$$
\begin{aligned}
\boldsymbol{g}_{\alpha I} &= \int_{\Gamma_C}^{*} \Psi_I \boldsymbol{p}^{[p-2]} n_\alpha d\Gamma - \int_{\Omega_C}^{*} \Psi_I \boldsymbol{p}_{,\alpha}^{[p-2]} d\Omega \\
&= \sum_{S=1}^{n_S} \left(\begin{aligned} &\Psi_I(\boldsymbol{\xi}_S)\boldsymbol{p}^{[p-2]}(\boldsymbol{\xi}_S)n_\alpha(\boldsymbol{\xi}_S)J^b(\boldsymbol{\xi}_S)\varpi_S^b \\ &-\Psi_I(\boldsymbol{\xi}_S)\boldsymbol{p}_{,\alpha}^{[p-2]}(\boldsymbol{\xi}_S)J(\boldsymbol{\xi}_S)\varpi_S^i \end{aligned} \right)
\end{aligned} \tag{79}
$$

$$
\begin{aligned}
\boldsymbol{g}_{\alpha\beta I} &= \int_{\Gamma_C}^{*} \Psi_{I,\alpha} \boldsymbol{p}^{[p-2]} n_\beta d\Gamma - \int_{\Gamma_C}^{*} \Psi_I \boldsymbol{p}_{,\beta}^{[p-2]} n_\alpha d\Gamma + \int_{\Omega_C}^{*} \Psi_I \boldsymbol{p}_{,\alpha\beta}^{[p-2]} d\Omega \\
&= \sum_{S=1}^{n_S} \left(\begin{aligned} &\Psi_{I,\alpha}(\boldsymbol{\xi}_S)\boldsymbol{p}^{[p-2]}(\boldsymbol{\xi}_S)n_\beta(\boldsymbol{\xi}_S)J^b(\boldsymbol{\xi}_S)\varpi_S^b \\ &-\Psi_I(\boldsymbol{\xi}_S)\boldsymbol{p}_{,\beta}^{[p-2]}(\boldsymbol{\xi}_S)n_\alpha(\boldsymbol{\xi}_S)J^b(\boldsymbol{\xi}_S)\varpi_S^b \\ &+\Psi_I(\boldsymbol{\xi}_S)\boldsymbol{p}_{,\alpha\beta}^{[p-2]}(\boldsymbol{\xi}_S)J(\boldsymbol{\xi}_S)\varpi_S^i \end{aligned} \right)
\end{aligned} \tag{80}
$$

accordingly, the components of force vector $\boldsymbol{f}$ can be evaluated by:

$$
\begin{aligned}
\boldsymbol{f}_I &= \int_{\Gamma^t}^{*} \Psi_I \bar{\boldsymbol{t}} d\Gamma - \int_{\Gamma^m}^{*} \Psi_{I,\alpha} \boldsymbol{a}_3 \boldsymbol{a}^\alpha \cdot \bar{\boldsymbol{m}} d\Gamma + \int_{\Omega}^{*} \Psi_I \bar{\boldsymbol{b}} d\Omega \\
&= \sum_{C=1}^{n_C} \left(\int_{\Gamma^t \cap \Gamma_C}^{*} \Psi_I \bar{\boldsymbol{t}} d\Gamma - \int_{\Gamma^m \cap \Gamma_C}^{*} \Psi_{I,\alpha} \boldsymbol{a}_3 \boldsymbol{a}^\alpha \cdot \bar{\boldsymbol{m}} d\Gamma + \int_{\Omega_C}^{*} \Psi_I \bar{\boldsymbol{b}} d\Omega \right) \\
&= \sum_{C=1}^{n_C} \sum_{S=1}^{n_S} \left(\begin{aligned} &\Psi_I(\boldsymbol{\xi}_S)\bar{\boldsymbol{t}}(\boldsymbol{\xi}_S)J^b(\boldsymbol{\xi}_S)\varpi_S^b \\ &-\Psi_{I,\alpha}(\boldsymbol{\xi}_S)\boldsymbol{a}_3(\boldsymbol{\xi}_S)\boldsymbol{a}^\alpha(\boldsymbol{\xi}_S)\cdot\bar{\boldsymbol{m}}(\boldsymbol{\xi}_S)J^b(\boldsymbol{\xi}_S)\varpi_S^b \\ &+\Psi_I(\boldsymbol{\xi}_S)\bar{\boldsymbol{b}}(\boldsymbol{\xi}_S)J(\boldsymbol{\xi}_S)\varpi_S^i \end{aligned} \right)
\end{aligned} \tag{81}
$$

It is noted that, in reproducing kernel gradient smoothing framework, the traditional meshfree shape functions and their first order gradients are only computed at the integration points of blue cycles. As we can find from the Table 1, the blue-cycle points are positioned at the boundary of triangular cells, such that the evaluation of meshfree shape function can share by more neighboring integration cells. As a result, the costly computation of meshfree shape functions can reduce from a global view.

5. Numerical Results

In this section, we present a set of numerical examples to validate the accuracy of the proposed methodology. The conventional L^2 and energy errors are used for convergence

study:

$$L^2\text{-Error} = \frac{\|\boldsymbol{v} - \boldsymbol{v}^h\|_{L^2}}{\|\boldsymbol{v}\|_{L^2}}, \quad H^{Energy}\text{-Error} = \frac{\|\boldsymbol{v} - \boldsymbol{v}^h\|_{H^{energy}}}{\|\boldsymbol{v}\|_{H^{energy}}} \tag{82}$$

In numerical examples, "GI-k" means the traditional Galerkin meshfree methods with kth-order Gauss quadrature rule, and "RKGSI" represent using the proposed reproducing kernel gradient smoothing integration.

5.1 Accuracy studies with manufactured solution

(a) 1D curved beam problem

(b) 2D shell problem

5.2 Pure bending problem for curved beam

Consider a pure bending curved beam problem as shown in Fig. 1, which can be regarded as a 1D reduction for shell problems. The configuration of the curved beam is depicted by the parametric coordinates $\{\xi^i\}_{i=1,2}$, and the left end of shell ($\xi^1 = 0$) is fixed, the right end ($\xi^1 = 1$) is applied a unit moment $\bar{M}$. The dimensionless geometric and material parameters for this problem are: radius $r = 1$, cross section with $A = 1$ and moment of inertia $I = 1/12$, Young's modulus $E = 12 \times 10^6$. According to Castigliano's theorem, the displacement components in directions of covariant basis $\boldsymbol{a}_\alpha$'s are listed as follows:

$$\begin{cases} v^1(x) = \dfrac{\bar{M}r^2}{EI}(\sin\dfrac{\xi^1}{r} - \dfrac{\xi^1}{r}) \\ v^2(x) = \dfrac{\bar{M}r^2}{EI}(1 - \sin\dfrac{\xi^1}{r}) \end{cases} \tag{83}$$

For this problem, the progressively refined meshfree discretizations with 11, 21, 41, 81 nodes are used for convergence assessment. The normalized support sizes for kernel function are 2.5, 3.5 and 4.5 for the quadratic, cubic, quartic basis functions. Figures 1-3 present the convergence results of L^2 and energy error norms, which clearly show that

Fig. 7. Description of the 1D rod problem

For this problem, meshfree discretizations with 11, 21, 41, 81, 161, and 321 nodes are employed for the convergence study. The normalized support sizes of 2.5 and 3.5 are utilized for the quadratic and cubic meshfree formulations, respectively. Figures 8-11 present the convergence results referring to the L^2 and H^1 error norms, where the horizontal axis "s" denotes the support size, and the dashed lines illustrate the numerical CR. It is evident that the Gauss integration rules, such as GI-2, GI-4 and GI-8 for quadratic formulation and GI-3, GI-6 and GI-9 for cubic formulation, could not produce the expected optimal convergence rates for L^2 and H^1 error norms, namely, 3 and 2 for the quadratic case and 4 and 3 for the cubic case, respectively. These observations can be explained by the inequalities of 错误!未找到引用源。 and 错误!未找到引用源。, where for the Gauss quadrature rules we have $p = 2$ and $q = 0$ for quadratic formulation and $p = 3$ and $q = 0$ for the cubic formulation. Consequently, following the inequalities of 错误!未找到引用源。 and 错误!未找到引用源。 as well as Table 1, it turns out that the solution errors of GI's are dominated by the integration error rather than the interpolation error. Even very high order quadrature rule like GI-8 only enables the optimal convergence of quadratic meshfree formulation for the initial coarse discretizations, where the interpolation error outplays the integration error for relatively larger nodal distance. However, when the discretizations are refined, the overall convergence of meshfree formulation is gradually governed by the integration error, i.e., for smaller nodal distance, the integration error becomes larger than the interpolation error. Therefore, the solutions computed by GI's are eventually controlled by the integration errors because these methods violate the integration consistency condition or integration constraint. The numerical results also evince that the ultimate convergence rates of GI's are slightly higher than $(q + 1)$ for L^2-error and q for H^1-error. This is perhaps due to the fact that the proposed theoretical development of error estimates relies on the conventional polynomial assumption and the meshfree shape functions actually are rational. This observation is also revealed by the interpolation error estimate of 错误!未找到引用源。, i.e., the interpolation order is often slightly higher than the basis degree in practice [1-8]. On the other hand, in case of the quadratic and cubic meshfree formulations with RKGSI, we have $q = p = 2$ and $q = p = 3$ in the inequalities of 错误!未找到引用源。 and

错误!未找到引用源。. Thus, as shown in Figs. 8-11, optimal convergence results regarding both L^2 and H^1 error norms are achieved by RKGSI, which fully agree with the theoretical results in Table 1.

Fig. 8. L^2-error convergence comparison for the 1D rod problem using quadratic meshfree formulation

Fig. 9. H^1-error convergence comparison for the 1D rod problem using quadratic meshfree formulation

Fig. 10. L^2-error convergence comparison for the 1D rod problem using cubic meshfree formulation

Fig. 11. H^1-error convergence comparison for the 1D rod problem using cubic meshfree formulation

5.2 Scordelis-Lo roof problem

As shown in Fig. 12, consider a 2D potential problem in a square domain with a length of $L=1$, where the left and the bottom sides are Neumann boundaries, and the right and the top sides are essential boundaries. The prescribed boundary values and the source term of this problem is computed according to following manufactured exact solution:

$$u(\boldsymbol{x}) = \sin(\frac{\pi}{2L}x)\sin(\frac{\pi}{2L}y) \tag{84}$$

Fig. 12. Description of the 2D square domain potential problem

Six progressively refined meshfree discretizations with 6×6, 11×11, 21×21, 41×41, 81×81 and 161×161 nodes are employed for the convergence assessment of this problem, where the first three discretizations are listed in Fig. 13. In the quadratic

and cubic meshfree methods, normalized support sizes of 2.5 and 3.5 are adopted for the kernel function. The convergence results of this 2D square domain potential problem are plotted in Figs. 14 and 15 for the quadratic meshfree formulation, and Figs. 16 and 17 for the cubic meshfree formulation, respectively. Similar to the previous 1D results, it is apparent from Figs. 14 and 15 that the results of GI-3 and GI-6 are completely governed by the integration errors, even GI-13 only produces better convergent results for very coarse discretizations, and this convergence is lost with refined discretizations. For the cubic case as listed in Figs. 16 and 17, all three GI methods including GI-6, GI-12 and GI-16 are not capable of achieving optimally convergent results. Figures. 16-17 also indicate that the convergence rates of all numerical results by GI's are approximately 1.5 for L^2-error and 0.5 for H^1-error, no matter what meshfree basis functions and GI quadrature rules are used. These results closely follow the theoretical predictions in Table 1, which gives 1 and 0 for the slopes of L^2 and H^1 errors because GI's do not meet the integration consistency and $q = 0$. As mentioned earlier, the small deviation between the theoretical and numerical convergence rates might attribute to the rational meshfree shape functions. Meanwhile, the numerical results of RKGSI in Figs. 14-17 unanimously support the optimal convergence rates of Galerkin meshfree methods listed in Table 1, namely, $(p+1)$ and p with respect to L^2 and H^1 errors.
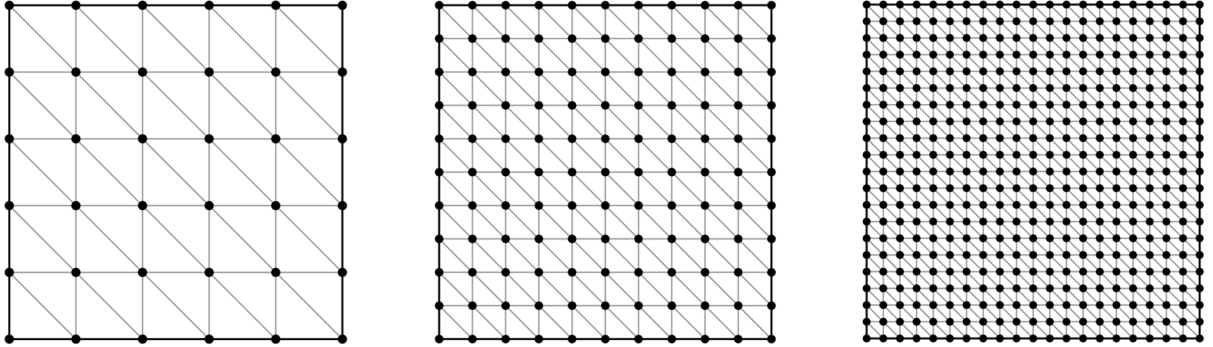

Fig. 13. Meshfree discretizations for the 2D square domain potential problem: 36, 121 and 441 nodes

Fig. 14. L^2-error convergence comparison for the 2D square domain potential problem using quadratic meshfree formulation

Fig. 15. H^1-error convergence comparison for the 2D square domain potential problem using quadratic meshfree formulation

Fig. 16. L^2-error convergence comparison for the 2D square domain potential problem using cubic meshfree formulation

Fig. 17. H^1-error convergence comparison for the 2D square domain potential problem using cubic meshfree formulation

5.3 Pinched hemisphere problem

As shown in Fig. 18, an infinite elastic plate with a circular hole is subjected to a x-direction far field load of $T=1000$. Under the plane stress condition, the analytical solution for this problem [80] is:

$$\begin{cases} u_x = \dfrac{Ta}{8\mu}[\dfrac{r}{a}(\kappa+1)\cos\theta + \dfrac{2a}{r}((1+\kappa)\cos\theta + \cos 3\theta) - \dfrac{2a^3}{r^3}\cos 3\theta] \\ u_y = \dfrac{Ta}{8\mu}[\dfrac{r}{a}(\kappa-3)\sin\theta + \dfrac{2a}{r}((1-\kappa)\sin\theta + \sin 3\theta) - \dfrac{2a^3}{r^3}\sin 3\theta] \end{cases} \tag{85}$$

in which (r,θ) are the polar coordinates, $\mu = E/2/(1+\nu)$, $\kappa = (3-\nu)/(1+\nu)$, E and ν are the Young's modulus and Poisson's ratio, respectively. During the computation, by taking the symmetry advantage, only a finite-size quarter model is analyzed, exact displacement and symmetric boundary conditions are enforced as shown in Fig. 18. The dimensionless geometric and material parameters are: length $L=4$, hole radius $a=1$, Young's modulus $E=2\times10^7$, Poisson ratio $\nu=0.3$.

Fig. 18. Description of the elastic plate with a circular hole problem

For this elastic plate with a circular hole problem, non-uniform meshfree discretizations using 104, 362, 1373, 5345 and 21089 nodes are utilized for the convergence study, where the first three progressively refined discretizations are portrayed in Fig. 19. The quadratic basis function with a normalized support size of 2.1 is employed to construct meshfree shape functions. The convergence results are

presented in Fig. 20 for the L^2-error and in Fig. 21 for the H^1-error, which again confirm that GI's lose the optimal convergence and this issue cannot be well remedied by just increasing the number of Gauss integration points. A direct comparison in Figs. 20 and 21 shows that optimal convergence rates of 3 and 2 are ensured by RKGSI for both L^2 and H^1 error norms.

Fig. 19. Meshfree discretizations for the elastic plate with a circular hole problem: 104, 362 and 1373 nodes

Fig. 20. L^2-error convergence comparison for the elastic plate with a circular hole problem using quadratic meshfree formulation

Fig. 21. H^1-error convergence comparison for the elastic plate with a circular hole problem using quadratic meshfree formulation

5.4 Hyperbolic paraboloid problem

To further assess the proposed theoretical results, a 3D cubic domain potential problem as shown in Fig. 22 is investigated. This cube has a unit length for all three directions, and a manufactured solution of $u(\boldsymbol{x}) = \exp(x + y + z)$ is taken as the exact solution. On the boundary surfaces of $x = 0$, $y = 0$, $z = 0$, essential boundary conditions are applied and the natural boundary conditions are imposed on the rest of surfaces. All prescribed boundary values are evaluated in accordance with the exact solution. Meshfree discretizations of $5 \times 5 \times 5$, $7 \times 7 \times 7$, $9 \times 9 \times 9$, $13 \times 13 \times 13$, $17 \times 17 \times 17$, and $25 \times 25 \times 25$ nodes are adopted for the convergence analysis of Galerkin meshfree methods, where the first three node distributions are plotted in Fig. 23. The normalized support sizes are 2.1 and 3.1 for quadratic and cubic meshfree formulations. The convergence results for this 3D cubic domain potential problem are given in Figs. 24-27, which reveal that for both quadratic and cubic meshfree formulations, high order Gauss integration rules such as GI-14 and GI-20 exhibit the same convergence behaviors as the relatively lower order rules GI-4 and GI-11 for quadratic and cubic cases, since all of them fail to meet the integration consistency condition. In contrast to GI's, as demonstrated in Figs. 24-27, RKGSI has the inherent property of integration

consistency and yields optimally convergent results for both L^2 and H^1 errors, which signifies the importance of integration consistency for Galerkin meshfree analysis.

Fig. 22. Description of the 3D cubic domain potential problem

Fig. 23. Meshfree discretizations for the 3D cubic domain potential problem: 125, 343 and 729 nodes

Fig. 24. L^2-error convergence comparison for the 3D cubic domain potential problem using quadratic meshfree formulation

Fig. 25. H^1-error convergence comparison for the 3D cubic domain potential problem using quadratic meshfree formulation

Fig. 26. L^2-error convergence comparison for the 3D cubic domain potential problem using cubic meshfree formulation

Fig. 27. H^1-error convergence comparison for the 3D cubic domain potential problem using cubic meshfree formulation

The last numerical example is a 3D hollow cylinder potential problem as described in Fig. 28. This hollow cylinder has a height of $L=1$ and its inner and outer radii are $r_i=1$ and $r_o=2$. Due to the symmetry, a quarter hollow cylinder is modelled, where natural boundary conditions are applied at $x=0$, $y=0$, and the rest of surfaces are subjected to essential boundary conditions. The prescribed values of both essential and natural boundary conditions are computed according to the following manufactured exact solution:

$$u(\boldsymbol{x}) = \sin(\pi \frac{r-r_i}{r_o-r_i}) \cos(\pi \frac{z}{L}) \tag{86}$$

This 3D hollow cylinder potential problem is analyzed by the cubic meshfree formulation with non-uniform meshfree discretizations of 225, 637, 1377, 4225 and 9537 nodes, and Fig. 29 lists the first three discretizations. The normalized support size of cubic meshfree shape functions is set to be 3.1. The convergence results for L^2 and H^1 errors are depicted in Figs. 30 and 31. It can be clearly seen that the convergence rates of GI's are far below the optimal convergence rates, namely, 4 for the L^2-error and 3 for the H^1-error. Once again, the results produced by GI-11, GI-14 and GI-20 show the same convergence trends as the meshfree models are progressively refined, which agree with the theoretical results stated in Table 1 and further assert that the convergence characteristics of meshfree formulation with GI's are deteriorated by the integration error. Meanwhile, the theoretically expected optimal convergent rates for L^2 and H^1 errors are congruently produced by RKGSI for this 3D hollow cylinder potential problem using non-uniform meshfree discretizations.

Fig. 28. Description of the 3D hollow cylinder potential problem

Fig. 29. Meshfree discretizations for the 3D hollow cylinder potential problem: 66, 231 and 861 nodes

Fig. 30. L^2-error convergence comparison for the 3D hollow cylinder potential problem using cubic meshfree formulation

Fig. 31. H^1-error convergence comparison for the 3D hollow cylinder potential problem using cubic meshfree formulation

6. Conclusions

A consistent integration scheme based upon reproducing kernel gradient smoothing (RKGS) framework is present for thin shell Galerkin meshfree formulation. In this approach, both first and second order gradients of meshfree shape functions are replaced by smoothed gradients in Galerkin weak form, where, with the aid of reproducing kernel gradient smoothing framework, the integration consistency becomes a natural property for smoothed gradients. For a supplement of traditional integration constraint, the integration consistency for thin shell problems is redefined as a condition that ensuring Galerkin methods perform an optimal behavior in energy error consisted with that obtained by interpolation. It is turns out that, for thin shell problems, the second order gradients of shape functions require p th order integration consistency, but only $(p-1)$ th order is sufficient for first order gradients. Under this circumstance, the first and second order smoothed gradients can be constructed with the same order of basis function by RKGS framework, while a set of particular numerical integration schemes with sufficient accuracy can be simultaneously used for the implements of first

and second order smoothed gradients. During the implement of smoothed gradients, the costly second order gradients of shape functions are eliminated, instead, only tradition shape functions and their gradients are required by RKGS framework. For a further improvement of efficiency, a set of optimal integration schemes are employed for assembly of force vector and smoothed gradients, in which the integration points used in force vector are located by minimizing the total number from a global point of view, and thus the calculation of shape functions and their first order gradients can reduce to a lower level. On the contrary, with the nature of integration consistency in smoothed gradients, the low order Gauss integration rules consisted with the order of the basis functions can be successfully adopted for assembly of stiffness matrix, and the results with optimal convergent behavior can always exist.

A set of numerical examples ranging from quadratic basis to quartic basis have been studied and demonstrate that the proposed RKGSI for thin shell is more accurate and efficient than traditional Gauss integration rule. and even better than meshfree interpolation.

Acknowledgements

Appendix

$$\boldsymbol{\Gamma}_{\alpha\beta} = \frac{\partial^2 \boldsymbol{r}}{\partial \xi^\alpha \partial \xi^\beta} = \boldsymbol{\Gamma}_{\beta\alpha}, \quad \Gamma^\gamma_{\alpha\beta} = \boldsymbol{\Gamma}_{\alpha\beta} \cdot \boldsymbol{a}^\gamma \tag{87}$$

$$\begin{aligned}
\boldsymbol{a}_{3,\alpha} &= \frac{1}{J} \boldsymbol{a}_{1,\alpha} \times \boldsymbol{a}_2 + \frac{1}{J} \boldsymbol{a}_1 \times \boldsymbol{a}_{2,\alpha} \\
&= \Gamma^i_{1\alpha} \frac{1}{J} \boldsymbol{a}_i \times \boldsymbol{a}_2 + \Gamma^i_{2\alpha} \frac{1}{J} \boldsymbol{a}_1 \times \boldsymbol{a}_i \\
&= \Gamma^\gamma_{\alpha\gamma} \boldsymbol{a}_3 - \Gamma^3_{\alpha\gamma} \boldsymbol{a}^\gamma
\end{aligned} \tag{88}$$

$$\kappa_{\alpha\beta} = \frac{1}{2} \left(\boldsymbol{a}_{3,\alpha} \cdot \boldsymbol{v}_{,\beta} + \boldsymbol{v}_{,\alpha} \cdot \boldsymbol{a}_{3,\beta} + \boldsymbol{a}_\alpha \cdot \boldsymbol{\varphi}_{,\beta} + \boldsymbol{\varphi}_{,\alpha} \cdot \boldsymbol{a}_\beta \right) \tag{89}$$

$$\begin{aligned}
\boldsymbol{a}_{3,\alpha} \cdot \boldsymbol{v}_{,\beta} &= (\boldsymbol{a}_3 \cdot \boldsymbol{v}_{,\beta})_{,\alpha} - \boldsymbol{a}_3 \cdot \boldsymbol{v}_{,\alpha\beta} \\
\boldsymbol{v}_{,\alpha} \cdot \boldsymbol{a}_{3,\beta} &= (\boldsymbol{v}_{,\alpha} \cdot \boldsymbol{a}_3)_{,\beta} - \boldsymbol{a}_3 \cdot \boldsymbol{v}_{,\alpha\beta} \\
\boldsymbol{\varphi}_{,\alpha} &= -(\boldsymbol{v}_{,\gamma} \cdot \boldsymbol{a}_3 \boldsymbol{a}^\gamma)_{,\alpha} \\
&= -\boldsymbol{v}_{,\alpha\gamma} \cdot \boldsymbol{a}_3 \boldsymbol{a}^\gamma - \boldsymbol{v}_{,\gamma} \cdot \boldsymbol{a}_{3,\alpha} \boldsymbol{a}^\gamma - \boldsymbol{v}_{,\gamma} \cdot \boldsymbol{a}_3 \boldsymbol{a}^\gamma_{,\alpha} \\
&= -\boldsymbol{v}_{,\alpha\gamma} \cdot \boldsymbol{a}_3 \boldsymbol{a}^\gamma - ((\boldsymbol{v}_{,\gamma} \cdot \boldsymbol{a}_3)_{,\alpha} - \boldsymbol{a}_3 \cdot \boldsymbol{v}_{,\alpha\gamma}) \boldsymbol{a}^\gamma - \boldsymbol{v}_{,\gamma} \cdot \boldsymbol{a}_3 \boldsymbol{a}^\gamma_{,\alpha} \\
&= -(\boldsymbol{v}_{,\gamma} \cdot \boldsymbol{a}_3)_{,\alpha} \boldsymbol{a}^\gamma - \boldsymbol{v}_{,\gamma} \cdot \boldsymbol{a}_3 \boldsymbol{a}^\gamma_{,\alpha} \\
\boldsymbol{a}_\alpha \cdot \boldsymbol{\varphi}_{,\beta} &= -\boldsymbol{a}_\alpha \cdot ((\boldsymbol{v}_{,\gamma} \cdot \boldsymbol{a}_3)_{,\beta} \boldsymbol{a}^\gamma + \boldsymbol{v}_{,\gamma} \cdot \boldsymbol{a}_3 \boldsymbol{a}^\gamma_{,\beta}) \\
&= -(\boldsymbol{v}_{,\alpha} \cdot \boldsymbol{a}_3)_{,\beta} - \boldsymbol{v}_{,\gamma} \cdot \boldsymbol{a}_3 \boldsymbol{a}^\gamma_{,\beta} \cdot \boldsymbol{a}_\alpha \\
&= -(\boldsymbol{v}_{,\alpha} \cdot \boldsymbol{a}_3)_{,\beta} + \Gamma^\gamma_{\alpha\beta} \boldsymbol{v}_{,\gamma} \cdot \boldsymbol{a}_3 \\
\boldsymbol{a}^\gamma_{,\beta} \cdot \boldsymbol{a}_\alpha &= (\boldsymbol{a}^\gamma \cdot \boldsymbol{a}_\alpha)_{,\beta} - \boldsymbol{a}^\gamma \cdot \boldsymbol{a}_{\alpha,\beta} = -\Gamma^\gamma_{\alpha\beta} \\
\boldsymbol{\varphi}_{,\alpha} \cdot \boldsymbol{a}_\beta &= -(\boldsymbol{v}_{,\beta} \cdot \boldsymbol{a}_3)_{,\alpha} + \Gamma^\gamma_{\alpha\beta} \boldsymbol{v}_{,\gamma} \cdot \boldsymbol{a}_3
\end{aligned} \tag{90}$$

$$\begin{aligned}
\kappa_{\alpha\beta} &= \frac{1}{2} \left(\boldsymbol{a}_{3,\alpha} \cdot \boldsymbol{v}_{,\beta} + \boldsymbol{v}_{,\alpha} \cdot \boldsymbol{a}_{3,\beta} + \boldsymbol{a}_\alpha \cdot \boldsymbol{\varphi}_{,\beta} + \boldsymbol{\varphi}_{,\alpha} \cdot \boldsymbol{a}_\beta \right) \\
&= \frac{1}{2} \left\{ \begin{array}{l} (\boldsymbol{a}_3 \cdot \boldsymbol{v}_{,\beta})_{,\alpha} - \boldsymbol{a}_3 \cdot \boldsymbol{v}_{,\alpha\beta} + (\boldsymbol{v}_{,\alpha} \cdot \boldsymbol{a}_3)_{,\beta} - \boldsymbol{a}_3 \cdot \boldsymbol{v}_{,\alpha\beta} \\ -(\boldsymbol{v}_{,\alpha} \cdot \boldsymbol{a}_3)_{,\beta} + \Gamma^\gamma_{\alpha\beta} \boldsymbol{v}_{,\gamma} \cdot \boldsymbol{a}_3 - (\boldsymbol{v}_{,\beta} \cdot \boldsymbol{a}_3)_{,\alpha} + \Gamma^\gamma_{\alpha\beta} \boldsymbol{v}_{,\gamma} \cdot \boldsymbol{a}_3 \end{array} \right\} \\
&= (\Gamma^\gamma_{\alpha\beta} \boldsymbol{v}_{,\gamma} - \boldsymbol{v}_{,\alpha\beta}) \cdot \boldsymbol{a}_3
\end{aligned} \tag{91}$$

$$\kappa_{\alpha\beta} = \frac{1}{2}(\boldsymbol{a}_{3,\alpha}\cdot\boldsymbol{v}_{,\beta} + \boldsymbol{v}_{,\alpha}\cdot\boldsymbol{a}_{3,\beta} + \boldsymbol{a}_\alpha\cdot\boldsymbol{\varphi}_{,\beta} + \boldsymbol{\varphi}_{,\alpha}\cdot\boldsymbol{a}_\beta)$$

$$= \frac{1}{2}((\boldsymbol{a}_3\cdot\boldsymbol{v}_{,\beta})_{,\alpha} + (\boldsymbol{v}_{,\alpha}\cdot\boldsymbol{a}_3)_{,\beta}) - \boldsymbol{a}_3\cdot\boldsymbol{v}_{,\alpha\beta}$$

$$+ \frac{1}{2}((\boldsymbol{a}_\alpha\cdot\boldsymbol{\varphi})_{,\beta} + (\boldsymbol{\varphi}\cdot\boldsymbol{a}_\beta)_{,\alpha}) - \boldsymbol{\varphi}\cdot\boldsymbol{a}_{\alpha\beta} \tag{92}$$

$$\boldsymbol{\varphi}\cdot\boldsymbol{a}_{\alpha\beta} + \boldsymbol{a}_3\cdot\boldsymbol{v}_{,\alpha\beta} = \boldsymbol{a}_3\cdot\boldsymbol{v}_{,\alpha\beta} - \boldsymbol{v}_{,\gamma}\cdot\boldsymbol{a}_3\Gamma^\gamma_{\alpha\beta} = \boldsymbol{a}_3\cdot(\boldsymbol{v}_{,\alpha\beta} - \boldsymbol{v}_{,\gamma}\Gamma^\gamma_{\alpha\beta})$$

$$= (\boldsymbol{a}_3\cdot\boldsymbol{v}_{,\alpha})_{,\beta} - \boldsymbol{a}_{3,\beta}\cdot\boldsymbol{v}_{,\alpha} - \boldsymbol{v}_{,\gamma}\Gamma^\gamma_{\alpha\beta}$$

$$\boldsymbol{a}_{3,\beta}\cdot\boldsymbol{v}_{,\alpha} + \boldsymbol{a}_{3,\alpha}\cdot\boldsymbol{v}_{,\beta} + 2\boldsymbol{v}_{,\gamma}\Gamma^\gamma_{\alpha\beta} \tag{93}$$

$$\frac{1}{2}(\boldsymbol{a}_{3,\alpha}\cdot\boldsymbol{v}_{,\beta} + \boldsymbol{v}_{,\alpha}\cdot\boldsymbol{a}_{3,\beta} - \boldsymbol{\varphi}\cdot(\boldsymbol{a}_{\alpha,\beta} + \boldsymbol{a}_{\beta,\alpha}))$$

$$= \frac{1}{2}(\boldsymbol{a}_{3,\alpha}\cdot\boldsymbol{v}_{,\beta} + \boldsymbol{v}_{,\alpha}\cdot\boldsymbol{a}_{3,\beta}) - \boldsymbol{v}_{,\gamma}\cdot\boldsymbol{a}_3\Gamma^\gamma_{\alpha\beta} \tag{94}$$

$$= \frac{1}{2}((\boldsymbol{a}_3\cdot\boldsymbol{v}_{,\beta})_{,\alpha} + (\boldsymbol{v}_{,\alpha}\cdot\boldsymbol{a}_3)_{,\beta}) - \boldsymbol{v}_{,\alpha\beta}\cdot\boldsymbol{a}_3 - \boldsymbol{v}_{,\gamma}\cdot\boldsymbol{a}_3\Gamma^\gamma_{\alpha\beta}$$

$$\kappa_{\alpha\beta} = \frac{1}{2}((\boldsymbol{\varphi}\cdot\boldsymbol{a}_\alpha)_{,\beta} + (\boldsymbol{\varphi}\cdot\boldsymbol{a}_\beta)_{,\alpha})$$

$$= \frac{1}{2}(\boldsymbol{\varphi}_{,\beta}\cdot\boldsymbol{a}_\alpha + \boldsymbol{\varphi}\cdot\boldsymbol{a}_{\alpha,\beta} + \boldsymbol{\varphi}_{,\alpha}\cdot\boldsymbol{a}_\beta + \boldsymbol{\varphi}\cdot\boldsymbol{a}_{\beta,\alpha}) \tag{95}$$

$$= \frac{1}{2}(\boldsymbol{\varphi}_{,\beta}\cdot\boldsymbol{a}_\alpha + \boldsymbol{\varphi}_{,\alpha}\cdot\boldsymbol{a}_\beta) + \frac{1}{2}(\boldsymbol{\varphi}\cdot\boldsymbol{a}_{\alpha,\beta} + \boldsymbol{\varphi}\cdot\boldsymbol{a}_{\beta,\alpha})$$

$$\boldsymbol{a}_{3,\alpha}\cdot\boldsymbol{v}_{,\beta} + \boldsymbol{v}_{,\alpha}\cdot\boldsymbol{a}_{3,\beta} - \boldsymbol{\varphi}\cdot\boldsymbol{a}_{\alpha,\beta} - \boldsymbol{\varphi}\cdot\boldsymbol{a}_{\beta,\alpha} = 0$$

$$= (\boldsymbol{a}_3\cdot\boldsymbol{v}_{,\beta})_{,\alpha} + (\boldsymbol{a}_3\cdot\boldsymbol{v}_{,\alpha})_{,\beta} - 2\boldsymbol{a}_3\cdot\boldsymbol{v}_{,\alpha\beta} - 2\boldsymbol{\varphi}\cdot\boldsymbol{a}^i\Gamma_{\alpha\beta} \tag{96}$$

$$\Gamma^\gamma_{\alpha\beta}\boldsymbol{a}_3 = \boldsymbol{a}_{\alpha,\beta}\cdot\boldsymbol{a}^\gamma\boldsymbol{a}_3 \tag{97}$$

$$\kappa_{\alpha\beta} = (\Gamma^\gamma_{\alpha\beta}\boldsymbol{u}_{,\gamma} - \boldsymbol{u}_{,\alpha\beta})\cdot\boldsymbol{a}_3 \tag{98}$$

$$\boldsymbol{g}^1 = \frac{1}{J}\boldsymbol{g}_2\times\boldsymbol{g}_3, \quad \boldsymbol{g}^2 = \frac{1}{J}\boldsymbol{g}_3\times\boldsymbol{g}_1, \quad \boldsymbol{g}^3 = \frac{1}{J}\boldsymbol{g}_1\times\boldsymbol{g}_2 \tag{99}$$

$$J = \boldsymbol{g}_1\cdot(\boldsymbol{g}_2\times\boldsymbol{g}_3) \tag{100}$$

$$\boldsymbol{g}^1 = \frac{1}{J}\boldsymbol{g}_2\times\boldsymbol{g}_3 = \frac{1}{J}(\boldsymbol{a}_2 + \xi^3\boldsymbol{a}_{3,2})\times\boldsymbol{a}_3 = \frac{1}{J}\boldsymbol{a}_2\times\boldsymbol{a}_3 = \boldsymbol{a}^1$$

$$\boldsymbol{g}^2 = \frac{1}{J}\boldsymbol{g}_3\times\boldsymbol{g}_1 = \frac{1}{J}\boldsymbol{a}_3\times(\boldsymbol{a}_1 + \xi^3\boldsymbol{a}_{3,1}) = \frac{1}{J}\boldsymbol{a}_3\times\boldsymbol{a}_1 = \boldsymbol{a}^2 \tag{101}$$

$$\int_{\Omega} \delta\varepsilon_{\alpha\beta} N^{\alpha\beta} d\Omega = \delta\boldsymbol{d}_I \cdot \int_{\Omega} \frac{1}{2}(\Psi_{I,\beta}\boldsymbol{a}_\alpha N^{\alpha\beta} + \Psi_{I,\alpha}\boldsymbol{a}_\beta N^{\alpha\beta}) d\Omega$$

$$= \delta\boldsymbol{d}_I \cdot \int_{\Gamma} \Psi_I \frac{1}{2}(\boldsymbol{a}_\alpha N^{\alpha\beta} n_\beta + \boldsymbol{a}_\beta N^{\alpha\beta} n_\alpha) d\Gamma \qquad (102)$$

$$-\delta\boldsymbol{d}_I \cdot \int_{\Omega} \Psi_I \frac{1}{2}((\boldsymbol{a}_\alpha N^{\alpha\beta})_{,\beta} + (\boldsymbol{a}_\beta N^{\alpha\beta})_{,\alpha}) d\Omega$$

$$\int_{\Omega} \delta\kappa_{\alpha\beta} M^{\alpha\beta} d\Omega = \int_{\Omega} (\Gamma^\gamma_{\alpha\beta} \delta\boldsymbol{v}_{,\gamma} - \delta\boldsymbol{v}_{,\alpha\beta}) \cdot \boldsymbol{a}_3 M^{\alpha\beta} d\Omega \qquad (103)$$

$$\int_{\Omega} \Gamma^\gamma_{\alpha\beta} \delta\boldsymbol{v}_{,\gamma} \cdot \boldsymbol{a}_3 M^{\alpha\beta} d\Omega = \int_{\Gamma} \delta\boldsymbol{v} \cdot \boldsymbol{a}_3 \Gamma^\gamma_{\alpha\beta} M^{\alpha\beta} n_\gamma d\Gamma - \int_{\Omega} \delta\boldsymbol{v} \cdot (\boldsymbol{a}_3 \Gamma^\gamma_{\alpha\beta} M^{\alpha\beta})_{,\gamma} d\Omega \qquad (104)$$

$$\int_{\Omega} \delta\boldsymbol{v}_{,\alpha\beta} \cdot \boldsymbol{a}_3 M^{\alpha\beta} d\Omega = \int_{\Gamma} \frac{1}{2}(\delta\boldsymbol{v}_{,\alpha} \cdot \boldsymbol{a}_3 n_\beta + \delta\boldsymbol{v}_{,\beta} \cdot \boldsymbol{a}_3 n_\alpha) M^{\alpha\beta} d\Omega - \int_{\Omega} \frac{1}{2}(\delta\boldsymbol{v}_{,\alpha} \cdot (\boldsymbol{a}_3 M^{\alpha\beta})_{,\beta} + \delta\boldsymbol{v}_{,\beta} \cdot (\boldsymbol{a}_3 M^{\alpha\beta})_{,\alpha}) d\Omega$$

$$= \int_{\Gamma} \frac{1}{2}(\delta\boldsymbol{v}_{,\alpha} \cdot \boldsymbol{a}_3 n_\beta + \delta\boldsymbol{v}_{,\beta} \cdot \boldsymbol{a}_3 n_\alpha) M^{\alpha\beta} d\Omega$$

$$-\int_{\Gamma} \frac{1}{2}(\delta\boldsymbol{v} \cdot (\boldsymbol{a}_3 M^{\alpha\beta})_{,\beta} n_\alpha + \delta\boldsymbol{v} \cdot (\boldsymbol{a}_3 M^{\alpha\beta})_{,\alpha} n_\beta) d\Gamma$$

$$+\int_{\Omega} \delta\boldsymbol{v} \cdot (\boldsymbol{a}_3 M^{\alpha\beta})_{,\alpha\beta} d\Omega$$

$$(105)$$

$$M^{\alpha\beta}_{,\beta} n_\alpha + M^{\alpha\beta}_{,\alpha} n_\beta + \Gamma^\gamma_{\alpha\beta} M^{\alpha\beta} n_\gamma \qquad (106)$$

$$\int_\Omega \frac{1}{2}((\boldsymbol{a}_3 \cdot \boldsymbol{v}_{,\alpha})_{,\beta} + (\boldsymbol{a}_3 \cdot \boldsymbol{v}_{,\beta})_{,\alpha})M^{\alpha\beta}d\Omega$$

$$= \int_\Gamma \frac{1}{2}((\boldsymbol{a}_3 \cdot \boldsymbol{v}_{,\alpha})n_\beta + (\boldsymbol{a}_3 \cdot \boldsymbol{v}_{,\beta})n_\alpha)M^{\alpha\beta}d\Gamma$$

$$- \int_\Omega \frac{1}{2}((\boldsymbol{a}_3 \cdot \boldsymbol{v}_{,\alpha})M^{\alpha\beta}_{,\beta} + (\boldsymbol{a}_3 \cdot \boldsymbol{v}_{,\beta})M^{\alpha\beta}_{,\alpha})d\Omega \qquad (107)$$

$$= \int_\Gamma \frac{1}{2}((\boldsymbol{a}_3 \cdot \boldsymbol{v}_{,\alpha})n_\beta + (\boldsymbol{a}_3 \cdot \boldsymbol{v}_{,\beta})n_\alpha)M^{\alpha\beta}d\Gamma$$

$$- \int_\Gamma \frac{1}{2}((\boldsymbol{a}_3 \cdot \boldsymbol{v})M^{\alpha\beta}_{,\beta}n_\alpha + (\boldsymbol{a}_3 \cdot \boldsymbol{v})M^{\alpha\beta}_{,\alpha}n_\beta)d\Gamma$$

$$+ \int_\Omega \boldsymbol{a}_3 \cdot \boldsymbol{v}M^{\alpha\beta}_{,\alpha\beta}d\Omega$$

$$\kappa_{\alpha\beta} = \frac{1}{2}(\boldsymbol{a}_{3,\alpha} \cdot \boldsymbol{v}_{,\beta} + \boldsymbol{v}_{,\alpha} \cdot \boldsymbol{a}_{3,\beta} + \boldsymbol{a}_\alpha \cdot \boldsymbol{\varphi}_{,\beta} + \boldsymbol{\varphi}_{,\alpha} \cdot \boldsymbol{a}_\beta)$$

$$= \frac{1}{2}((\boldsymbol{a}_3 \cdot \boldsymbol{v}_{,\alpha})_{,\beta} + (\boldsymbol{a}_3 \cdot \boldsymbol{v}_{,\beta})_{,\alpha}) \qquad (108)$$

$$= \frac{1}{2}(\boldsymbol{a}_{3,\beta} \cdot \boldsymbol{v}_{,\alpha} + \boldsymbol{a}_{3,\alpha} \cdot \boldsymbol{v}_{,\beta}) + \boldsymbol{a}_3 \cdot \boldsymbol{v}_{,\alpha\beta}$$

$$\frac{1}{2}(\boldsymbol{a}_{3,\beta} \cdot \boldsymbol{v}_{,\alpha} + \boldsymbol{a}_{3,\alpha} \cdot \boldsymbol{v}_{,\beta}) - \Gamma^\gamma_{\alpha\beta}\boldsymbol{v}_{,\gamma} \cdot \boldsymbol{a}_3$$

$$= \frac{1}{2}(\boldsymbol{a}_{3,\beta} \cdot \boldsymbol{v}_{,\alpha} + \boldsymbol{a}_{3,\alpha} \cdot \boldsymbol{v}_{,\beta}) - \Gamma^\gamma_{\alpha\beta}\boldsymbol{v}_{,\gamma} \cdot \boldsymbol{a}_3 \qquad (109)$$

$$\boldsymbol{a}_{3,\alpha} \cdot \boldsymbol{v}_{,\beta} - \Gamma^\gamma_{\alpha\beta}\boldsymbol{v}_{,\gamma} \cdot \boldsymbol{a}_3$$

References

1. T. Belytschko, Y. Kronggauz, D. Organ, M. Fleming, P. Krysl, Meshless methods: an overview and recent developments, *Computer Methods in Applied Mechanics and Engineering* 139 (1996) 3-47.

2. S.N. Atluri, S.P. Shen, *The Meshless Local Petrov–Galerkin (MLPG) Method*, Tech Science, 2002.

3. I. Babuška, U. Banerjee, J.E. Osborn, Survey of meshless and generalized finite element methods: a unified approach, *Acta Numerica* 12 (2003) 1-125.

4. S. Li, W.K. Liu, *Meshfree Particle Methods*, Springer-Verlag, 2004.

5. X. Zhang, Y. Liu, *Meshless Methods*, Tsinghua University Press & Springer-Verlag, 2004.

6. V.P. Nguyen, T. Rabczuk, S. Bordas, M. Duflot, Meshless methods: A review and computer implementation aspects, *Mathematics and Computers in Simulation* 79 (2008) 763-813.

7. G.R. Liu, *Meshfree Methods: Moving beyond The Finite Element Method (2nd Edition)*, CRC Press, 2009.

8. J.S. Chen, M. Hillman, S.W. Chi, Meshfree methods: progress made after 20 years, *Journal of Engineering Mechanics-ASCE* 143 (2017) 04017001.

9. B. Nayroles, G. Touzot, P. Villon, Generalizing the finite element method: Diffuse approximation and diffuse elements, *Computational Mechanics* 10 (1992) 307-318.

10. T. Belytschko, Y.Y. Lu, L. Gu, Element-free Galerkin methods, *International Journal for Numerical Methods in Engineering* 37 (1994) 229-256.

11. T. Belytschko, Y.Y. Lu, L. Gu, M. Tabbara, Element-free Galerkin methods for static and dynamic fracture, *International Journal of Solids and Structures* 32 (1995) 2547-2570.

12. W.K. Liu, S. Jun, Y.F. Zhang, Reproducing kernel particle methods, *International Journal for Numerical Methods in Fluids* 20 (1995) 1081-1106.

13. J.S. Chen, C. Pan, C.T. Wu, W.K. Liu, Reproducing kernel particle methods for large deformation analysis of nonlinear structures, *Computer Methods in Applied Mechanics and Engineering* 139 (1996) 195-227.

14. C.A. Duarte, J.T. Oden, An hp adaptive method using clouds, *Computer Methods in Applied Mechanics and Engineering* 139 (1996) 237-262.

15. I. Babuška, J.M. Melenk, The partition of unity method, *International Journal for Numerical Methods in Engineering* 40 (1997) 727-758.

16. N. Sukumar, B. Moran, T. Belytschko, The natural element method in solid mechanics, *International Journal for Numerical Methods in Engineering* 43 (1998) 839-887.

17. S.N. Atluri, T. Zhu, A new meshless local Petrov-Galerkin (MLPG) approach in computational mechanics, *Computational Mechanics* 22 (1998) 117-127.

18. J.G. Wang, G.R. Liu, A point interpolation meshless method based on radial basis functions, *International Journal for Numerical Methods in Engineering* 54 (2002) 1623-1648.

19. W.K. Liu, W. Han, H. Lu, S. Li, J. Cao, Reproducing kernel element method. Part I: Theoretical formulation, *Computer Methods in Applied Mechanics and Engineering* 193 (2004) 933-951.

20. N. Sukumar, Construction of polygonal interpolants: a maximum entropy approach, *International Journal for Numerical Methods in Engineering* 61 (2004) 2159-2181.

21. M. Arroyo, M. Ortiz, Local maximum-entropy approximation schemes: a seamless bridge between finite elements and meshfree methods, *International Journal for Numerical Methods in Engineering* 65 (2006) 2167-2202.

22. G.R. Liu, K.Y. Dai, T.T. Nguyen, A smoothed finite element method for mechanics problems, *Computational Mechanics*, 39 (2007) 859-877.

23. P.C. Guan, S.W. Chi, J.S. Chen, T.R. Slawson, M.J. Roth, Semi-Lagrangian reproducing kernel particle method for fragment-impact problems, *International Journal of Impact Engineering* 38 (2011) 1033-1047.

24. D. Wang, P. Chen, Quasi-convex reproducing kernel meshfree method, *Computational Mechanics* 54 (2014) 689-709.

25. P. Metsis, N. Lantzounis, M. Papadrakakis, A new hierarchical partition of unity formulation of EFG meshless methods, *Computer Methods in Applied Mechanics and Engineering* 283 (2015) 782-805.

26. E. Yreux, J.S. Chen, A quasi-linear reproducing kernel particle method, *International Journal for Numerical Methods in Engineering* 109 (2017) 1045-1064.

27. Y. Wu, C.T. Wu, Simulation of impact penetration and perforation of metal targets using the smoothed particle Galerkin method, *Journal of Engineering Mechanics-ASCE* 144 (2018) 04018057.

28. N. Trask, P. Bochev, M. Perego, A conservative, consistent, and scalable meshfree mimetic method, *Journal of Computational Physics* 409 (2020) 109187.

29. P. Lancaster, K. Salkauskas, Surfaces generated by moving least squares methods, *Mathematics of Computation* 37 (1981) 141-158.

30. J. Dolbow, T. Belytschko, Numerical integration of the Galerkin weak form in meshfree methods, *Computational Mechanics* 23 (1999) 219-230.

31. S. Beissel, T. Belytschko, Nodal integration of the element-free Galerkin method, *Computer Methods in Applied Mechanics and Engineering* 139 (1996) 49-74.

32. C.T. Dyka, P.W. Randles, R.P. Ingel, Stress points for tension instability in SPH, *International Journal for Numerical Methods in Engineering* 40 (1997) 2325-2341.

33. T. Rabczuk, T. Belytschko, S.P. Xiao, Stable particle methods based on Lagrangian kernels, *Computer Methods in Applied Mechanics and Engineering* 193 (2004) 1035-1063.

34. C.T. Wu, Y. Wu, Z. Liu, D. Wang, A stable and convergent Lagrangian particle method with multiple local stress points for large strain and material failure analysis. *Finite Elements in Analysis and Design* 146 (2018) 96-106.

35. R. Silva-Valenzuela, A. Ortiz-Bernardin, N. Sukumar, E. Artioli, N. Hitschfeld-Kahler, A nodal integration scheme for meshfree Galerkin methods using the virtual element decomposition, *International Journal for Numerical Methods in Engineering* 121 (2020) 2174-2205.

36. M. Hillman, J.S. Chen, An accelerated, convergent, and stable nodal integration in Galerkin meshfree methods for linear and nonlinear mechanics, *International Journal for Numerical Methods in Engineering* 107 (2016) 603-630.

37. S. De, K.J. Bathe, The method of finite spheres with improved numerical integration, *Computers & Structures* 79 (2001) 2183-2196.

38. A. Carpinteri, G. Ferro, G. Ventura, The partition of unity quadrature in meshless methods, *International Journal for Numerical Methods in Engineering* 54 (2002) 987-1006.

39. Y. Liu, T. Belytschko, A new support integration scheme for the weakform in mesh-free methods, *International Journal for Numerical Methods in Engineering* 82 (2010) 699-715.

40. J.S. Chen, C.T. Wu, S. Yoon, Y. You, A stabilized conforming nodal integration for Galerkin mesh-free methods, *International Journal for Numerical Methods in*

Engineering 50 (2001) 435-466.

41. J.S. Chen, S. Yoon, C.T. Wu, Non-linear version of stabilized conforming nodal integration for Galerkin mesh-free methods, *International Journal for Numerical Methods in Engineering* 53 (2002) 2587-2615.

42. B.M. Irons, A. Razzaque, Experience with the patch test for convergence of finite element methods, A.K. Aziz (Ed.), Mathematical Foundations of the Finite Element Method, Academic Press, London (1972), pp. 557-587.

43. O.C. Zienkiewicz, R.L.Taylor, The finite element patch test revisited a computer test for convergence, validation and error estimates, *Computer Methods in Applied mechanics and Engineering* 149 (1997) 223-254.

44. D. Wang, J.S. Chen, Locking-free stabilized conforming nodal integration for meshfree Mindlin-Reissner plate formulation, *Computer Methods in Applied mechanics and Engineering* 193 (2004) 1065-1083.

45. J.S. Chen, D. Wang, A constrained reproducing kernel particle formulation for shear deformable shell in Cartesian coordinates, *International Journal for Numerical Methods in Engineering* 68 (2006) 151-172.

46. D. Wang, J.S. Chen, A Hermite reproducing kernel approximation for thin-plate analysis with sub-domain stabilized conforming integration, *International Journal for Numerical Methods in Engineering* 74 (2008) 368-390.

47. D. Wang, Y. Wu, An efficient Galerkin meshfree analysis of shear deformable cylindrical panels, *Interaction and Multiscale Mechanics* 1 (2008) 339-355.

48. D. Wang, Z. Lin, Dispersion and transient analyses of Hermite reproducing kernel Galerkin meshfree method with sub-domain stabilized conforming integration for thin beam and plate structures, *Computational Mechanics* 48 (2011) 47-63.

49. D. Wang, H. Peng, A Hermite reproducing kernel Galerkin meshfree approach for buckling analysis of thin plates, *Computational Mechanics* 51 (2013) 1013-1029.

50. D. Wang, C. Song, H. Peng, A circumferentially enhanced Hermite reproducing kernel meshfree method for buckling analysis of Kirchhoff-Love cylindrical shells, *International Journal of Structural Stability and Dynamics* 15 (2015) 1450090.

51. D. Wang, Z. Li, L. Li, Y. Wu, Three dimensional efficient meshfree simulation of large deformation failure evolution in soil medium, *Science China Technological Sciences* 54 (2011) 573-580.

52. Y. Wu, D. Wang, C.T. Wu, Three dimensional fragmentation simulation of concrete structures with a nodally regularized meshfree method, *Theoretical and Applied Fracture Mechanics* 72 (2014) 89-99.

53. Y. Wu, D. Wang, C.T. Wu, H. Zhang, A direct displacement smoothing meshfree particle formulation for impact failure modeling, *International Journal of Impact Engineering* 87 (2016) 169-185.

54. D. Wang, J. Wang, J. Wu, J. Deng, M. Sun, A three dimensional two-level gradient smoothing meshfree method for rainfall induced landslide simulations, *Frontiers of Structural and Civil Engineering* 13 (2019) 337-352.

55. X.F. Pan, C.T. Wu, W. Hu, Y. Wu, A momentum-consistent stabilization algorithm for Lagrangian particle methods in the thermo-mechanical friction drilling analysis, *Computational Mechanics* 64 (2019) 625-644.

56. T.H. Huang, J.S. Chen, H. Wei, M. Roth, E.H. Fang, A MUSCL-SCNI approach for meshfree modeling of shock waves in fluids, C*omputational Particle Mechanics* 7 (2020)329-350 .

57. Q. Duan, X. Li, H. Zhang, T. Belytschko, Second-order accurate derivatives and integration schemes for meshfree methods, *International Journal for Numerical Methods in Engineering* 92 (2012) 399-424.

58. Q. Duan, X. Gao, B. Wang, X. Li, H. Zhang, T. Belytschko, Y. Shao, Consistent element-free Galerkin method, *International Journal for Numerical Methods in Engineering* 99 (2014) 79-101.

59. B. Wang, C. Lu, C. Fan, M. Zhao, Consistent integration schemes for meshfree analysis of strain gradient elasticity, *Computer Methods in Applied Mechanics and Engineering* 357 (2019) 112601.

60. J.S. Chen, M. Hillman, M. Rüter, An arbitrary order variationally consistent integration for Galerkin meshfree methods, *International Journal for Numerical Methods in Engineering* 95 (2013) 387-418.

61. M. Hillman, J.S. Chen, S.W. Chi, Stabilized and variationally consistent nodal integration for meshfree modeling of impact problems, *Computational Particle Mechanics* 1 (2014) 245-256.

62. D. Wang, J. Wu, An efficient nesting sub-domain gradient smoothing integration algorithm with quadratic exactness for Galerkin meshfree methods, *Computer Methods in Applied Mechanics and Engineering* 298 (2016) 485-519.

63. D. Wang, J. Wu, An inherently consistent reproducing kernel gradient smoothing

framework toward efficient Galerkin meshfree formulation with explicit quadrature, *Computer Methods in Applied Mechanics and Engineering* 349 (2019) 628-672.

64. J. Wu, D. Wang, Z. Lin, D. Qi, An efficient gradient smoothing meshfree formulation for the fourth-order phase field modeling of brittle fracture, *Computational Particle Mechanics* 7 (2020) 193-207.

65. G. Strang, Variational crimes in finite element method, in: A.K. Aziz (Ed.), *The Mathematical Foundations of the Finite Element Method with Applications to Partial Differential Equations*, Academic Press, 1972: pp. 689-710.

66. G. Strang, G. Fix, *An Analysis of the Finite Element Method*, Wellesley-Cambridge Press, 2018.

67. W.K. Liu, Y. Chen, C.T. Chang, T. Belytschko, Advances in multiple scale kernel particle methods, *Computational Mechanics* 18 (1996) 73-111.

68. W.K. Liu, S. Li, T. Belytschko, Moving least-square reproducing kernel methods (I) Methodology and convergence, *Computer Methods in Applied Mechanics and Engineering* 143 (1997) 113-154.

69. J.S. Chen, W. Han, Y. You, X. Meng, A reproducing kernel method with nodal interpolation property, *International Journal for Numerical Methods in Engineering* 56 (2003) 935-960.

70. W. Han, X. Meng, Error analysis of the reproducing kernel particle method, *Computer Methods in Applied Mechanics and Engineering* 190 (2001) 6157-6181.

71. I. Babuška, U. Banerjee, J.E. Osborn, Q. Li, Quadrature for meshless methods, *International Journal for Numerical Methods in Engineering* 76 (2008) 1434-1470.

72. M. Rüter, J. S. Chen, An enhanced-strain error estimator for Galerkin meshfree methods based on stabilized conforming nodal integration, *Computers & Mathematics with Applications* 74 (2017) 2144-2171.

73. S. Fernández-Méndez, A. Huerta, Imposing essential boundary conditions in mesh-free methods, *Computer Methods in Applied Mechanics and Engineering* 193 (2004) 1257-1275.

74. A. Quarteroni, A. Valli, *Numerical Approximation of Partial Differential Equations*, Springer, 1994.

75. P.J. Davis, P. Rabinowitz, *Methods of Numerical Integration*, Courier Corporation, 2007.

76. Philippe G., *Linear and Nonlinear Functional Analysis with Applications*, SIAM-Society for Industrial and Applied Mathematics, 2013.

77. R.L. Burden, J.D. Faires, *Numerical Analysis (9th Edition)*, Brooks Cole, 2010.

78. T.J.R. Hughes, *The Finite Element Method: Linear Static and Dynamic Finite Element Analysis*, Dover Publications, 2000.

79. O.C. Zienkiewicz, R.L. Taylor, J.Z. Zhu, *The Finite Element Method: Its Basis and Fundamentals (7th Edition)*, Elsevier, Singapore, 2015.

80. S.P. Timoshenko, J.N. Goodier, *Theory of Elasticity (3rd Edition)*, McGraw-Hill, 1970.